Exploring relationships between shock-induced microstructures and H₂O and Cl in apatite grains from eucrite meteorites

T.J. Barrett [a,*], A. Černok [a], G. Degli-Alessandrini [a], X. Zhao [a], M. Anand [a,b], I.A. Franchi [a], J.R. Darling [c]

[a] The Open University, School of Physical Sciences, Walton Hall, Milton Keynes MK7 6AA, UK
[b] Department of Earth Sciences, Natural History Museum, London SW7 5BD, UK
[c] University of Portsmouth, School of the Environment, Geography and Geosciences, Burnaby Road, Portsmouth PO1 3QL, UK

Abstract

The abundance and isotopic composition of volatile elements in meteorites is critical for understanding planetary evolution, given their importance in a variety of geochemical processes. There has been significant interest in the mineral apatite, which occurs as a minor phase in most meteorites and is known to contain appreciable amounts of volatiles (up to wt. % F, Cl, and OH). Impact-driven shock metamorphism, pervasive within many meteorites, can potentially modify the original signatures of volatiles through processes such as devolatilization and diffusion. In this study, we investigate the microstructures of apatite grains from six eucrites across a broad range of shock stages (S1–S5) using electron backscatter diffraction (EBSD) to explore shock-induced crystallographic features in apatite. New Cl and H abundance and isotopic composition data were collected on moderate to highly shocked samples (S3-S5) by Nano Secondary Ion Mass Spectrometry (NanoSIMS). Previously reported volatile data for S1 and S2 eucrites were integrated with EBSD findings in this study. Our findings indicate that apatite microstructures become increasingly more complex at higher shock stages. At low shock stages (S1–S2) samples display brecciation and fracturing of apatite. Samples in S3 and S4 display increasing crystal plastic deformation indicated by increasing spread in pole figures. At the higher shock stages (S4/S5) there is potential recrystallisation demonstrated by an increased density of subgrain boundaries. The Cl content and δ^{37}Cl values of highly-shocked apatite grains range from ∼940 to 1410 ppm and −3.38 to +7.70‰, respectively, within the range observed in less-shocked eucrites. In contrast, H₂O abundances are more variable (from 186 to ∼4010 ppm), however, the measured water content still falls within the range previously reported for low-shock eucrites. The measured δD values range from −157 to +163‰, also within the range of values from known low-shock basaltic eucrites. Weighted averages for both isotopic systems (δD −122 ± 20‰, δ^{37}Cl + 1.76 ± 0.66‰) are consistent with the range displayed in other inner Solar System bodies. NanoSIMS isotope images of apatite grains display heterogeneity in their Cl abundance at the nanoscale which increases in complexity with shock stage. This increasing complexity, however, does not correlate with deformation microstructures observed in EBSD or with the Cl isotopic composition at either an inter-grain or intra-grain scale. These findings are similar to analyses of variably shocked lunar apatite and, therefore, apatite appears to be a robust recorder of Cl and H (at least at spatial resolution and precision currently achievable by NanoSIMS) on airless bodies, despite intensive shock.
© 2021 The Authors. Published by Elsevier Ltd. This is an open access article under the CC BY license (http://creativecommons.org/licenses/by/4.0/).

Keywords: Apatite; Volatiles; Hydrogen; Chlorine; Shock; EBSD; NanoSIMS; Eucrites

* Corresponding author.
    E-mail address: thomas.barrett@open.ac.uk (T.J. Barrett).

1. INTRODUCTION

The Howardite-Eucrite-Diogenite (HED) meteorites comprise the largest suite of crustal and sub-crustal rocks available from a differentiated basaltic asteroid (likely 4 Vesta) (e.g. McSween et al., 2013). The eucrites, which are composed primarily of plagioclase and pigeonite, are also some of the oldest basaltic igneous rocks in the Solar System (typical ages range from 4547 to 4559 million years (Ma) with 2σ uncertainties usually ranging from 5 to 13 Ma; Misawa et al., 2005; Zhou et al., 2013; Touboul et al., 2015). As such, understanding the evolution of volatile elements (e.g. hydrogen and chlorine), their abundance, and isotopic composition within these samples can provide insight into the origin of volatiles, the material accreted into differentiated bodies, and primary/secondary processes that operated on asteroid parent bodies early in Solar System history (e.g. Barrett et al., 2016, 2019; Sarafian et al., 2017a, 2017c; Stephant et al., 2021). These elements, however, can undergo fractionation during the evolution of the parent body (e.g. magma ocean degassing, eruption, large impact-melt sheet degassing; Roszjar et al., 2011; Sarafian et al., 2017b; Alexander et al., 2018; McCubbin and Barnes, 2019) potentially masking their original signature. Despite this, each isotope system can provide unique and complementary perspectives on these important processes.

Owing to the large difference in relative mass between hydrogen (^1H) and deuterium (^2H or D), it is possible for significant fractionation to occur. It is because of this significant fractionation that H isotopes can be used to 'fingerprint' source(s) of water and/or any processes that may have affected the sample (e.g. Hallis, 2017). The hydrogen isotopic composition of the inner Solar System is highly variable, ranging over several orders of magnitude, from near protosolar in composition ($\delta D \sim -700\permil$, D/H $\sim 4.67 \times 10^{-5}$, please see methods Section 3.3.2 for derivation of the standard delta 'δ' notation in per mil) to several thousand per mil in the martian atmosphere ($\delta D > +3000\permil$, D/H $> 6.23 \times 10^{-4}$) (McCubbin and Barnes, 2019 and references therein).

The chlorine isotopic composition, on the other hand, is relatively restricted for terrestrial rocks, martian meteorites, and all chondritic meteorites groups ($\delta^{37}Cl \sim -5.6$ to $+3.8\permil$, although one data point for a martian meteorite does reach $+8.6\permil$, please see Section 3.3.1 for derivation of $\delta^{37}Cl$) (e.g. Sharp et al., 2013, 2016; Bellucci et al., 2017). Samples from both the Moon and eucrites (likely from 4 Vesta), however, display a significant range in Cl isotopic composition potentially related to degassing at various points within their histories ($\delta^{37}Cl \sim -4$ to $+81.1\permil$ and ~ -4 to $+39\permil$, respectively)(e.g. Boyce et al., 2015; Barnes et al., 2016; Sarafian et al., 2017b; Barrett et al., 2019; Wang et al., 2019).

Apatite $[Ca_5(PO_4)_3(F, Cl, OH)]$ is a common phosphate mineral in planetary materials, known to contain appreciable amounts of volatiles (up to wt.% levels F, Cl, and OH; e.g. Hallis et al., 2012b; Barnes et al., 2014; Bellucci et al., 2017; Sarafian et al., 2017b). As such, apatite has been of significant interest in assessing the volatile evolution of various bodies within the Solar System via in-situ analytical techniques such as Secondary Ion Mass Spectrometry (SIMS) (e.g. Hallis, 2017; Shearer et al., 2018; McCubbin and Barnes, 2019). Whilst previous works considered the geological context of the apatite grain and the surrounding mineralogy (e.g. Potts et al., 2016), less attention has been given to understanding as to how the internal structure of apatite and its volatile inventory may be influenced by thermal metamorphism (Sarafian et al., 2019; Stephant et al., 2021) and shock deformation (Černok et al., 2019, 2020; Darling et al., 2021).

The HEDs can be subdivided petrologically into basaltic eucrites (basalts), cumulate eucrites (gabbros), polymict eucrites (breccias of basaltic and sometimes cumulate eucrites), diogenites (orthopyroxenites, occasional harzburgites, and rare dunites and norites), and howardites (polymict breccias composed of eucrites and diogenites some of which contain elevated noble gas contents, owing to solar wind implantation, indicative of being a regolith; Warren et al., 2009; McSween et al., 2019). The basaltic eucrites, which are the most common of all eucrites, are typically fine to medium-grained igneous rocks, composed mainly of pigeonite and calcic plagioclase (ranging from bytownite to anorthite; Mittlefehldt, 2015). Cumulate eucrites are thought to be mixtures of cumulus minerals (pyroxene and plagioclase) and trapped melt whose parent magmas were similar to basaltic eucrites (Treiman, 1997; Barrat et al., 2000; Mittlefehldt and Lindstrom, 2003; Barrat, 2004).

Basaltic eucrites can be further characterised based on their bulk chemical compositions into a Main Group-Nuevo Laredo (hereafter referred to as Main Group), the incompatible element rich Stannern trend, and the incompatible element depleted residual eucrites (e.g., Stolper, 1977; Mayne et al., 2009; Yamaguchi et al., 2013). The Main Group comprises the majority of the basaltic eucrites and is widely accepted as a fractional crystallisation trend (Stolper, 1977; Warren and Jerde, 1987; Mittlefehldt and Lindstrom, 2003). The Stannern trend eucrites have similar major element abundances to Main Group eucrites but have higher abundances of Ti and incompatible elements, enrichments that are not linked to Mg# (Barrat et al., 2000; Hutchison, 2004; Barrat et al., 2007). Barrat et al. (2007) suggested that the contamination of Main Group eucrites by crustal melts could explain both the elevated incompatible element concentrations and the distinctive Eu, Sr, and Be anomalies shown by Stannern trend eucrites. This crustal partial melt would leave behind a residuum with LREE depletion, which Yamaguchi et al. (2009) observed in several eucrites and believed to be a third geochemical trend dubbed the 'residual eucrites'.

When classifying eucrites for thermal metamorphism, Takeda and Graham (1991) separated the eucrites into six types (1–6) based on the characteristics of pyroxene. Type one represents the lowest level of thermal metamorphism indicated by extensively zoned pyroxene; conversely, type six pyroxene contain easily resolvable exsolution lamellae with some pigeonite grains inverting to orthopyroxene. Later, Yamaguchi et al. (1996) suggested an additional type seven and that thermal metamorphism by burial led to global metamorphism which could explain the different

metamorphic types by their position within the crust during this event. Sarafian et al. (2019) studied the volatile content in unequilibrated eucrites to minimise the possibility of diffusive resetting of primordial volatiles. Their work found the volatile content did not vary from core-to-rim and the D/H ratio of the measured clinopyroxene was within error of the D/H ratios of apatite, concluding that the water accreted to Vesta was from a carbonaceous chondrite source. More recently, work by Stephant et al. (2021) expanded the data available for eucrite clinopyroxene, finding lighter δD values than corresponding apatite and suggest that at least some of water in Vesta was derived from a relatively deuterium-poor reservoir in the protosolar nebula.

The eucrites, like many meteorite samples, have been shocked, to varying degrees, during their history and it is unclear how this may have influenced the volatile inventory of these rocks. Shock effects in meteorites comprise two major phenomena: 1) Shock deformation, defined as the mechanical deformation of rocks below or above the solidus caused by compression stress generated by hypervelocity impacts (Bischoff and Stöffler, 1992) and 2) post shock thermal metamorphism. Both shock-induced phenomena have the potential to mobilise volatile elements, and thus modify the original (magmatic) H and Cl signatures in apatite through processes such as phase transformation and diffusion (e.g. Higashi et al., 2017; Wang et al., 2017). If shock-induced volatile mobility is not properly assessed and accounted for, it may lead to potentially erroneous interpretations of the origin and distribution of volatile elements in the Solar System.

An impact shock scale for meteorites based on ordinary chondrites was first introduced by Stöffler et al. (1991) with samples classified from unshocked (S1) to very strongly shocked (S6). More recently Fritz et al. (2017), then Stöffler et al. (2018) revised this scale, adding focus to localised melt zones as well as separating classifications schemes for different rock types (mafic, felsic etc.). Minerals can often record micro/nano scale structural changes in response to processes such as shock. Electron Backscatter Diffraction (EBSD) analyses provide crystallographic information at the μm and sub-μm length scales. The technique is commonly used in terrestrial geology to infer microstructural information, such as crystal lattice distortions, based on the analysis of the crystallographic orientation and misorientation of grains (e.g. Prior et al., 1999, 2009). EBSD, however, has not been widely used to study planetary materials, especially phosphates. When EBSD has been used on extraterrestrial samples, it has mostly been used to identify new minerals (e.g. Ma and Beckett, 2021), interpret plastic deformation and magnetic measurements (e.g. Tkalcec et al., 2013; Tkalcec and Brenker, 2014; Forman et al., 2017; Nichols et al., 2018), crystallographic preferred orientations (e.g. Daly et al., 2019; Tkalcec and Brenker, 2019), and shock deformation in geochronometers such as zircon and baddeleyite (e.g. Darling et al., 2016). Importantly, the latter studies highlighted the importance of EBSD as a tool for understanding deformation at the μm- and nm-scale for interpreting complex U-Pb data and for accounting for the mobility of Pb, a moderately volatile element. Černok et al. (2019) provided the first

insights into the shock-induced microstructures of lunar apatite and merrillite, observing that internal microstructures become progressively more complex (increasing internal misorientation and formation of subgrains) and deformed with increasing levels of shock-loading. Additional work by Cox et al. (2020) noted the variability in response to shock deformation of apatite in the peak ring of the Chicxulub impact crater. More recently, Kumler and Day (2021) assessed the trace element and moderately volatile element behaviour of eucrites, finding impact processes do not have a pronounced effect on the abundances of moderately volatile elements and suggest that Vesta has a more heterogenous distribution of volatile elements and is similarly to slightly less volatile-depleted than the Moon.

Experimental work has demonstrated relatively rapid H-diffusion in apatite grains subject to elevated temperatures, which is of significance for apatite exposed to high post-shock temperatures commonly associated with high shock pressure (Brenan, 1993; Higashi et al., 2017). Brenan (1993) demonstrates that diffusion typically occurs as halogen exchange. In the case of Higashi et al. (2017), the authors experimentally model the isotopic diffusion of H in a Durango fluorapatite with a saturated $^2H_2O/O_2$ vapor and provide an average H diffusion coefficient at 500 °C of $2.56 \pm 0.79 \times 10^{-18}$ m/s. These reinforced observations of impact-associated volatile mobility within martian (Howarth et al., 2015) and terrestrial (Kenny et al., 2020) apatite. Furthermore, Černok et al. (2020) investigated the potential link between deformation-induced microstructures and the isotopic composition of volatiles in apatite from a suite of Apollo lunar samples representing the ancient crustal rocks from the Moon. Their work suggested that despite samples experiencing a wide range of shock-deformation, water-rich apatite (>100 ppm H_2O) appears to retain the original isotopic signature of H in the Moon. In contrast, chlorapatite in a highly-shocked martian meteorite (S5-S6) records micro- to nano-scale chlorine heterogeneities that directly correlate with shock deformation and recrystallisation features (estimates range from 29 GPa to >42 GPa for basaltic shergottite Northwest Africa 5298; Darling et al., 2021). Additionally, the hydrogen isotopic composition of martian apatite and silicate minerals from other studies have variable δD values from $\sim-80‰$ to $\sim+4600‰$, indicative of magmatic water mixing with the extremely enriched martian atmosphere which could potentially be shock induced (e.g. Greenwood et al., 2008; Hallis et al., 2012a; Hu et al., 2014).

Currently, it is unclear whether lunar samples reflect the full range of shock microstructures for samples from airless bodies within our collection; given no studies have investigated how deformation-induced microstructures may influence the abundance and isotopic composition of volatiles (such as Cl or H) in apatite from eucrites, this work provides useful insight into shock effects on small, airless, differentiated bodies. The ancient crystallisation ages of the eucrites mean they can also provide details regarding processes affecting volatile reservoirs early on in Solar System history and the nature of the material that provided these volatiles to differentiated bodies. In this study we

analyse the microstructures of apatite grains from eucrite samples with a wide range of shock stages (S1-S5) and investigate any potential relationship with their respective volatile signatures. Where no literature shock stage or data is provided, shock stages are assigned to samples based on petrographic observations. The three lower shock samples (Dar al Gani (DaG) 945, Millbillillie, and Stannern) have had their H and Cl isotopic composition measured previously (Barrett et al., 2016, 2019) and these values, many of which are from the exact grains mapped using EBSD here, have been integrated into this studies data evaluation and interpretation.

2. SAMPLE DESCRIPTION

Table 1 provides an overview of the samples studied in this paper, of which four are observed falls and two are finds. Three of the samples (DaG 945, Millbillillie, Stannern) have had their mineralogy previously described in Barrett et al. (2016, 2019) for the specific apatite grains analysed here. The mineralogical and textural context of new samples (Cachari, Padvarninkai, and Puerto Lápice) are described below including a brief overview of the other samples. Representative back-scattered electron (BSE) images illustrating the textural and petrological context of the apatite analysed in this study are provided in Fig. 1 and the supplementary material. These samples were selected as they are mostly observed falls and therefore unlikely to have experienced significant terrestrial weathering, are well characterised in terms of their petrology, thermal history (e.g. pyroxene metamorphic grade; types 4–6 being common among the eucrites), and for some their shock history (Cachari, Puerto Lápice), and finally, several have published H and Cl isotopic data to allow direct comparison to this study (Cachari, DaG 945, Millbillillie, Stannern).

2.1. Dar al Gani 945 (S1)

DaG 945 is a coarse-grained, residual eucrite with a granulitic texture predominately consisting of subhedral pyroxene and plagioclase with some more fine-grained relict mesostasis regions. Minor phases in DaG 945 include: apatite, chromite, ilmenite, a silica polymorph, and zircon, all of which typically occur in late-stage mesostasis pockets. Yamaguchi et al. (2009) note that whilst both pyroxene and plagioclase can preserve igneous zonation (therefore a type 4 eucrite), DaG 945 also displays well-defined 120° triple junctions indicative of significant localised recrystallisation in BSE images.

2.2. Cachari (S4)

Cachari is a heavily-shocked, coarse-grained monomict basaltic eucrite find composed mainly of mosaicised pyroxene, plagioclase, and vesicular impact melt veins (Fredriksson and Kraut, 1967; Bogard et al., 1985). Pyroxene show typical exsolution and plagioclase are known to have mottled extinction in cross-polarised light (Bogard et al., 1985). Early work by Fredriksson and Kraut (1967) suggested that, in close proximity to the melt veins, plagioclase was partly altered to maskelynite, however, the later work of Bogard et al. (1985) suggested that no alteration had occurred. Fritz et al. (2017) highlight that maskelynite formation can occur at lower pressures with increasing Ca-content and given plagioclase in this sample are calcic ($\sim An_{88}$; Fredriksson and Kraut, 1967) it could be possible there is some localised maskelynite formation. It is more likely, however, that partially isotropic plagioclase was observed, which is a key indicator of the high-grade S4 shock stage (Fritz et al., 2017). From this assessment, Cachari is considered to have experienced a shock stage of S4 (high). Other minor phases include ilmenite, merrillite, and zircon. Age data from Bogard et al. (1985) using the ^{39}Ar-^{40}Ar system, provide a ~3.0 Ga impact age for the sample.

Sarafian et al. (2014) measured a single apatite grain for its H isotopes in Cachari and found it to have a H isotope composition similar to other measured eucrites ($-158 \pm 24‰$ 2σ). The Cl isotope composition for Cachari was measured first by Sarafian et al. (2017b) with values ranging from $2.35 \pm 0.45‰$ (2σ) to $6.41 \pm 0.50‰$ with an average composition of $4.87 \pm 2.25‰$.

Table 1
Main characteristics of the meteorites studied. SG = Shock stage based on the Stöffler et al. (1991) scale, MG = Thermal metamorphic grade based on the pyroxene thermal scale (Takeda and Graham, 1991; Yamaguchi et al., 1996). Cosmic ray exposure (CRE) ages for eucrites Stannern and Millbillillie are taken from Miura et al. (1998); Puerto Lápice (Llorca et al., 2009); Cachari (Eugster and Michel, 1995). EBSD protocol 1 refers to the high beam current conditions used in the analysis of samples with literature volatile data. EBSD protocol 2 refers to the lower beam current conditions used to obtain EBSD maps without volatile mobilisation prior to isotopic analysis. For more details on the EBSD protocol please see Section 3.2.

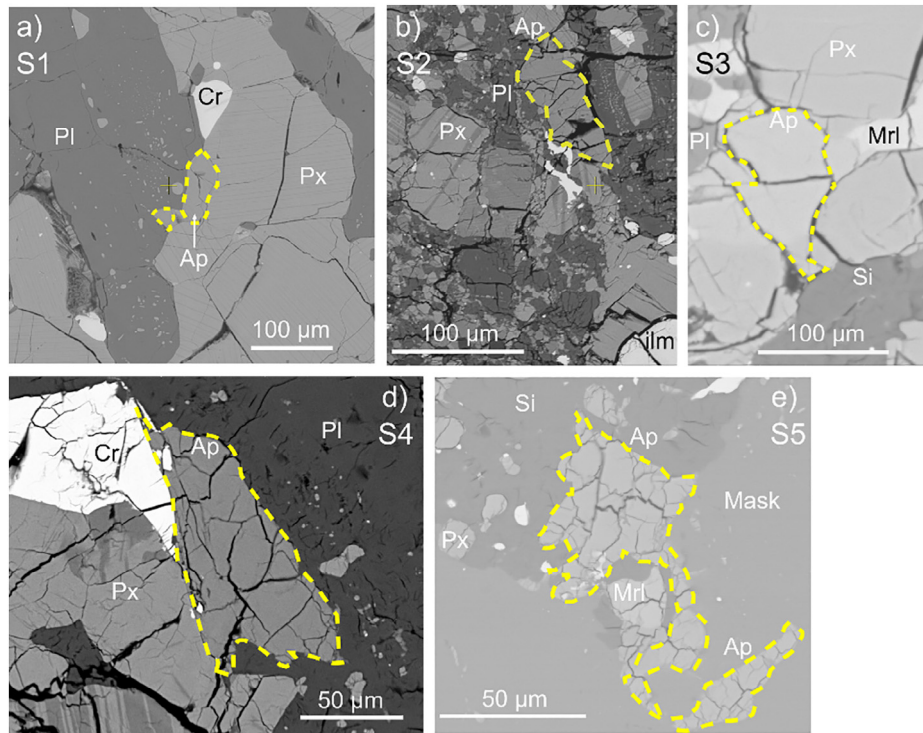| Meteorite	Find/Fall	Geochemical Trend	CRE Age (Ma)	SG	GPa (If Known)	MG	EBSD Protocol	Note
Cacahri	Find	Main Group	8.3	S4			2	
DaG 945	Find	Residual	-	S1		4	1	
Millbillillie	Fall	Main Group	20.08	S2		6	1	
Padvarninkai	Fall	Main Group	-	S5	42–60	5	2	
Puerto Lápice	Fall	Main Group	19.0	S3	~15	6?	2	Rare localised up to 30 GPa
Stannern	Fall	Stannern Trend	35.1	S2		4	1	

Fig. 1. Representative backscatter electron (BSE) maps of apatite grains and their surroundings. Yellow dashed lines outline the studied apatite grains. (a) DaG 945 (S1), (b) Millbillillie (S2), (c) Puerto Lápice (S3), (d) Cachari (S4), (e) Padvarninkai (S5). BSE images indicates fragmentation of apatite grains (e.g., S4) but do not provide any indication on the internal microstructural complexities of the apatite crystal structure that occur as a response to increasing deformation (S2 and higher). Ap = apatite, Cr = chromite, ilm = ilmenite, Mask = maskelynite, Mrl = merrillite, Px = pyroxene, Pl = plagioclase, Si = silica phase.

2.3. Millbillillie (S2)

Millbillillie is a main group, polymict eucrite which consists of two dominant rock types. The first lithology is a fine-grained, subophitic, basaltic texture where interstitial pyroxene has recrystallised to a fine-grained granoblastic texture (Yamaguchi et al., 1994). The second lithology is a coarse-grained breccia (Bobe et al., 1989; Yamaguchi et al., 1994, 1996). Overall, pyroxene in this sample is type 6. Minor phases occur in both lithologies and include chromite, phosphates (apatite and merrillite), ilmenite, a silica polymorph, troilite, and zircon. Hopkins et al. (2015) provides a ^{207}Pb-^{206}Pb age of a zircon core at 4555 ± 17 Ma, in agreement with earlier works (Bukovanská et al., 1997; Miura et al., 1998).

2.4. Padvarninkai (S5)

Padvarninkai is a monomict eucrite fall originally classified as a shergottite by Binns (1967) on the basis of the presence of maskelynite before Mason et al. (1979) showed its chemical composition is identical to eucrites and later confirmation by oxygen isotope analysis (Greenwood et al., 2005). The sample consists of two main lithologies: a fine to coarse-grained unbrecciated lithology and impact melt veins. Pyroxenes are severely fractured and mosaicked type 5 pigeonite and despite the shock textures, the igneous texture is still well preserved. Plagioclase is ophitic and mostly

converted to maskelynite. Minor phases include fluorapatite, chromite, ilmenite, a silica phase and troilite. Given the strong shock features, it is believed this sample is the most shocked eucrite in the eucrite meteorite collection and the work of Bischoff and Stöffler (1992) to estimate the equilibrium shock pressure to be between 42 and 60 GPa (S5). The weighted mean ^{207}Pb/^{206}Pb age as recorded by zircon and baddeleyite is 4553 ± 13 Ma (Bukovanská et al., 1997).

2.5. Puerto Lápice (S3)

Puerto Lápice is a relatively recent eucrite fall (Castilla-La Mancha, Spain, 10 May 2007) with a detailed description of the petrology and chemistry given by Llorca et al. (2009). Puerto Lápice is a brecciated main group eucrite which contains a variety of lithologies including basaltic and granulitic clasts, breccia fragments, and recrystallised impact melt (Llorca et al., 2009). Given the pyroxene exsolution lamella observed in backscatter electron (BSE) images in this study and the presence of orthopyroxene (Llorca et al., 2009), the sample can nominally be categorised to have a thermal metamorphic grade of type 6. The sample is also reported to contain shock melt veins which provide evidence for at least three separate shock events (Llorca et al., 2009). These veins, however, are not observed in the thin section studied here. Llorca et al. (2009) provide a maximum shock pressure for the whole rock of ~15 GPa, assigning Puerto Lápice S3 shock stage,

based on the undulose extinction of plagioclase with no planar deformation features and strong undulose extinction of pyroxene with planar and irregular fractures. The authors, however, recognise highly localised areas near the melt veins have experienced pressures up to 30 GPa based on the presence of maskelynite (Llorca et al., 2009) which is not observed in the thin section studied here. An average cosmic ray spallation age for the sample is 19 ± 2 Ma (Llorca et al., 2009) suggesting this sample could belong to the eucrite exposure cluster identified at either 21 ± 4 Ma (Eugster and Michel, 1995) or 22 ± 2 Ma (Shukolyukov and Begemann, 1996). The Pu-Xe age date for this sample (20 ± 19 Ma younger than the reference Angra dos Reis with an absolute age 4.5578 ± 0.0004 Ga from Lugmair and Galer, 1992, giving Puerto Lápice an age of ~4.537 Ga) is typical for eucrites (Llorca et al., 2009).

2.6. Stannern (S2)

The Stannern eucrite lends its name to the Stannern trend group of eucrites believed to be the result of contamination by crustal partial melts (Barrat et al., 2007). Stannern itself is a monomict breccia with a subophitic texture and type 4 pyroxene. Fine-grained mesostasis pockets also occur in this sample interstitially between large (up to several mm in the longest axis) laths of plagioclase. Minor phases include phosphate (apatite and merrillite), chromite, ilmenite, troilite, a silica polymorph, and zircon.

3. METHODS

3.1. Optical and scanning electron microscopy

Initial observations were conducted using a Zeiss Axioplan petrographic microscope at The Open University in plane-polarised and cross-polarised light. Observations were made to identify minerals based on their optical properties, ascertain the petrographic context of apatite, and investigate mineral shock features where possible.

To locate appropriate apatite grains (i.e. large enough grains with sufficient crack-free areas for isotope analyses) each polished thin-section was carbon-coated using an EMITECH K950X Turbo carbon sputter coater and examined at The Open University using a Quanta 200 3D Scanning Electron Microscope (SEM) fitted with an Oxford Instruments 80 mm^2 X-Max Energy Dispersive X-ray (EDX) detector. An electron beam with an acceleration voltage of 20 kV and a beam current of 0.6 nA was used for the acquisition of all the BSE images and elemental X-ray maps to avoid potential mobilisation of volatiles (much less than the 4 nA suggested as the threshold of volatile mobilisation; Goldoff et al., 2012; Barnes et al., 2013). Whole-section elemental EDS maps were acquired for each sample and correlated hotspots of Ca and P X-ray lines were used to locate phosphates (typically <100 μm), which were later investigated by spot-mode (exposure ~30 s) to distinguish between apatite and merrillite [$(Mg,Fe)_2REE_2Ca_{16}P_{14}O_{56}$]. Once located, high-resolution BSE and secondary electron (SE) images of the phosphates were collected to aid in subsequent analyses.

3.2. Electron Backscatter Diffraction (EBSD)

Following SEM analysis, the carbon coat was removed using isopropanol and/or 0.25 μm diamond paste. The sample was then polished with 0.06 μm colloidal silica on a multicloth (both purchased from Metprerp) for ~15 min using a LabPol-5 system at 150 rpm, with a LabForce-1 head and an automated closer. Polishing removes the mechanical damage layer from previous, coarser polishing grits as well as minimises scattering of the electron beam owing to surface topography, therefore improving the quality of the analyses. The crystallographic orientation and the internal deformation features (i.e. crystal lattice bending, low angle misorientation bands, subgrain boundaries) of the selected apatite grains were investigated using EBSD on a Zeiss Supra 55VP Field Emission (FEG)-SEM located at The Open University and equipped with an Oxford Instruments NordlysNano EBSD detector.

Samples were tilted to a 70° angle from the horizontal position for EBSD. Acquisition step size ranged from 300 nm to 750 nm, with binning of acquired Electron Backscatter Patterns (EBSPs) ranging from 2×2 pixels to 4×4 pixels. Generated EBSPs were matched to a hexagonal reference apatite data from (Wilson et al., 1999; a = 9.4555 Å, b = 9.4555 Å, c = 6.8836 Å and α = 90°, β = 90°, γ = 120°.). For apatite grains that had been previously analysed for their isotopic composition, an acceleration voltage of 20 kV, an aperture of 120 μm and a beam current of 9.1 nA (current pre-determined by use of a Faraday Cup under the same conditions) were used in high-vacuum mode and with a 30 nm carbon coat using the same carbon coater as noted earlier (EBSD protocol 1 in Table 1). EBSPs under these conditions were collected for between 5.4 and 25.0 ms.

For apatite grains for which no isotopic data were previously acquired, an acceleration voltage of 20 kV, an aperture of 30 μm, and a beam current of 565 pA (also pre-determined using a Faraday Cup) were used under low-vacuum mode (30 Pa, nitrogen atmosphere) and without a carbon coat (EBSD protocol 2 in Table 1). EBSPs were collected for between 26.3 and 526.3 ms. The latter beam conditions (20 kV, low beam current) are similar to Černok et al. (2019, 2020) and used to avoid any potential volatile element mobility that could compromise future isotopic analysis (e.g. Goldoff et al., 2012; Barnes et al., 2013).

EBSD results were processed using Oxford Instruments HKL Channel 5 software. Orientation data were cleaned of erroneous data by performing a routine single wild spike removal, followed by a seven-point iterative nearest neighbour zero solution (Forman et al., 2016). Wild spike replaces individual isolated indexed pixels with zero solutions and the seven-point nearest neighbour processing infills zero solutions with a computed solution/orientation based upon adjacent indexed pixels (in this case seven).

3.3. Nano secondary ion mass spectrometry (NanoSIMS) protocol

3.3.1. Chlorine isotope analysis
The Cl content and Cl isotopic compositions of apatite were measured using the Cameca NanoSIMS 50 L at The

Open University in scanning ion imaging mode using a modified protocol based on Stephant et al. (2019), acquiring negative secondary ions of ^{12}C, ^{18}O, ^{35}Cl, ^{37}Cl, and $^{40}Ca^{19}F$, simultaneously on electron multipliers with a mass resolving power of ~8000 (Cameca definition). Two data points in Puerto Lápice (PL-Ap1a, PL-Ap1b) were collected in multi-collection mode using the protocol outlined in Barrett et al. (2019). Prior to ion-probe analyses, the carbon coat used for SEM analysis was removed, and a ~30 nm thick gold coat applied. Samples were stored in a vacuum oven at ~55 °C for at least 24 hours prior to transfer to the NanoSIMS airlock. Once in the airlock, each sample was left to degas under vacuum at ~55 °C for at least another day before transferring it to the vessel chamber. The primary current ranged from 15–20 pA and provided a spatial resolution of ~200 nm. Mass $^{40}Ca^{19}F$ was monitored in real time imaging (RTI) mode to identify apatite grains prior to analyses. Monitoring ^{12}C ion beam intensities during analyses allowed the identification of cracks originally hidden beneath the surface. Typically, an 8 μm × 8 μm area was analysed, however, for some larger grains the area was increased to 10 μm × 10 μm. As analyses showed homogenous images of ^{18}O and ^{35}Cl in RTI mode; no electronic gating was used. Pulse height detection (PHD) adjustment was carried out at the start of each day for ^{18}O, ^{35}Cl, and ^{37}Cl and every few days for $^{40}Ca^{19}F$, to account for detector ageing.

Data were processed with the L'IMAGE software developed by Larry Nittler from the Carnegie Institute of Washington. The deadtime was set at 44 ns and corrected with L'IMAGE. Regions of interest (ROIs) were identified on each image based on the $^{40}Ca^{19}F/^{18}O$ and $^{35}Cl/^{18}O$ images. Terrestrial apatite standards (Ap004, Ap005, Ap018; see McCubbin et al., 2012) were used for calibration purposes in this study. Ap004 ($\delta^{37}Cl$ value of ~+0.11‰; Barnes et al., 2016) was used to correct for instrumental mass fractionation (IMF) of the measured isotope ratios. Ap004 and Ap018 were analysed together to produce a calibration curve of known Cl abundance versus $^{35}Cl/^{18}O$ ratio, from which the eucrite apatite Cl contents were calculated. Since the Cl isotopic composition for Ap018 is unknown, this standard was only used for abundance calibration. A nominally anhydrous San Carlos olivine and was used to assess the total background Cl contribution. The total background Cl was found to be ≪1 ppm for all sessions (typically 0.08–0.1 ppm) and the contribution removed from the results presented. The background contribution to the measured result was ≪1% (~6–9 × 10⁻³%). Work conducted on the same instrument by Barrett et al. (2019) demonstrated there is no evidence for an extreme isotopic composition of the background and as such no correction to the isotopic composition for background contribution was conducted. The measured $^{37}Cl/^{35}Cl$ ratios are corrected for the IMF and expressed in $\delta^{37}Cl$ notation as defined in Eq. (1), with standard mean ocean chloride $\delta^{37}Cl_{SMOC} = 0$ (Kaufmann et al., 1984). Errors estimated for $\delta^{37}Cl$ values take into consideration the error based on counting statistics, as well as the uncertainty associated with the IMF calculation.

$$\delta^{37}Cl = \left\{ \left(\frac{R_{sample}}{R_{SMOC}} \right) - 1 \right\} * 1000 \qquad (1)$$

3.3.2. Hydrogen spot analysis

Hydrogen analyses were conducted on top of the Cl pits using the same instrument following a well-established protocol (e.g. Barnes et al., 2014; Barrett et al., 2016). Prior to analysis, areas (typically 12 μm × 12 μm) containing target apatite grains were pre-sputtered to remove surface contamination, using a large Cs^+ primary beam of ~450 pA current with an acceleration voltage of 8 kV, the sample surface being at −8 kV. The instrument was set up in multi-collection mode, measuring negative secondary ions of ^1H, D, ^{12}C, and ^{18}O on electron multipliers with a mass resolving power of ~4300 (Cameca definition) sufficient to resolve $^1H_2^-$ from D^-. An electron flood gun was used to compensate for charge build up. For analysis, the raster area was reduced to a 10 μm × 10 μm area, with a 25 % electronic gating set in order to collect only secondary ions emitted from the central zone (5 μm × 5 μm) of the analysis area. For some analyses, however, the raster size needed to be reduced further down to 6 μm × 6 μm. Secondary ion images of ^1H and ^{12}C were monitored in real time during pre-sputtering to ensure that the area to be analyzed was free of cracks or hotspots indicative of contamination. Monitoring the ^1H and ^{12}C ion beam intensities during analyses allowed the identification of cracks originally hidden beneath the surface. In such cases, only portions of the secondary ion signals corresponding to analysis of pristine material were considered and isolated using the NanoSIMS Data Editor software (Frank Gyngard, Washington University). As noted in Tartèse et al. (2013) from the same laboratory, isolating portions of the signal makes no discernible difference in D/H and $^1H/^{18}O$ ratios when compared to the full integration for reference apatite grains. Standards Ap003, Ap004 and Ap018 (McCubbin et al., 2012) were used for the calibration purposes along with San Carlos. Background H_2O content ranged from 8 to 18 ppm across all days. Raw D/H ratios were corrected based on the percentage contribution of the instrument background to the measured H_2O content, and the δD value of the instrument background (−55 ± 100‰, based on 23 repeated measurements of San Carlos olivine), following the relationship outlined in Barrett et al. (2016). Samples were corrected for cosmic-ray spallation using lunar production rates (Merlivat et al., 1976) and using the known cosmic ray exposure (CRE) ages (Eugster and Michel, 1995; Llorca et al., 2009). Since the CRE age for Padvarninkai is currently unknown, this sample was corrected for the effects of spallation using the oldest grouping of CRE ages for HED meteorites (38 Ma) to evaluate the effect of the maximum possible spallation correction on its measured D/H ratio. Given the significant water content of the sample, the difference between this maximum correction and a younger CRE age estimate (8.1 Ma) is <1‰. The H isotope composition of apatite measured in this study is reported using the standard δD (per mil,‰) notation whereby:

$$\delta D = \left\{ \left(\frac{R_{sample}}{R_{VSMOW}} \right) - 1 \right\} * 1000 \qquad (2)$$

The reference used is VSMOW with a D/H ratio of 155.76×10^{-6} (Hagemann et al., 1970).

4. RESULTS

4.1. Textural context and shock-induced microstructures of apatite in eucrites

A total of 23 EBSD maps were collected for 27 apatite grains from six eucrites ranging from shock stages S1 to S5 (see Fig. 2 for a representative set of each shock stage, and supplementary material for full dataset). Some EBSD maps contain multiple apatite grains given their close proximity to each other but owing to the small and/or cracked nature of these apatite they were not analysed by SIMS. EBSD data are presented as band contrast (BC) images, grain reference orientation deviation (GROD) maps, inverse pole figures (IPF), pole figures (PF), and low angle grain boundary maps, with local misorientation maps in the supplementary material. Band contrast images visualise the overall quality of the EBSPs used to index the minerals in an EBSD map where whiter regions indicate areas of high pattern quality. Inverse pole figures indicate the crystallographic direction of the individual crystals parallel to the sample surface (Z0), whereas pole figures plot the {0 0 1} and {1 0 –1 0} pole to planes in upper hemisphere equal area stereographic projection. In GROD maps, the internal misorientation of each pixel relative to the grain average orientation is color-coded, where colder (blue) colours represent low deviations (1–2°) from the average and warmer (red) colours represent high deviations (9–10°) from the average (angular resolution of EBSD is <0.5°; Borthwick and Piazolo, 2010). The GROD maps (Fig. 2p–t) highlight the presence of subgrains and/or other structural complexities (e.g., strain, low angle grain boundaries) within the indexed mineral. Local misorientation maps (see supplementary material) provide information regarding the relative misorientation of a pixel to its neighbours (in this case a 5×5 square filter was used) with a similar colour scheme to the GROD maps. Subgrain boundaries are defined here by adjacent pixels with a low angle boundary
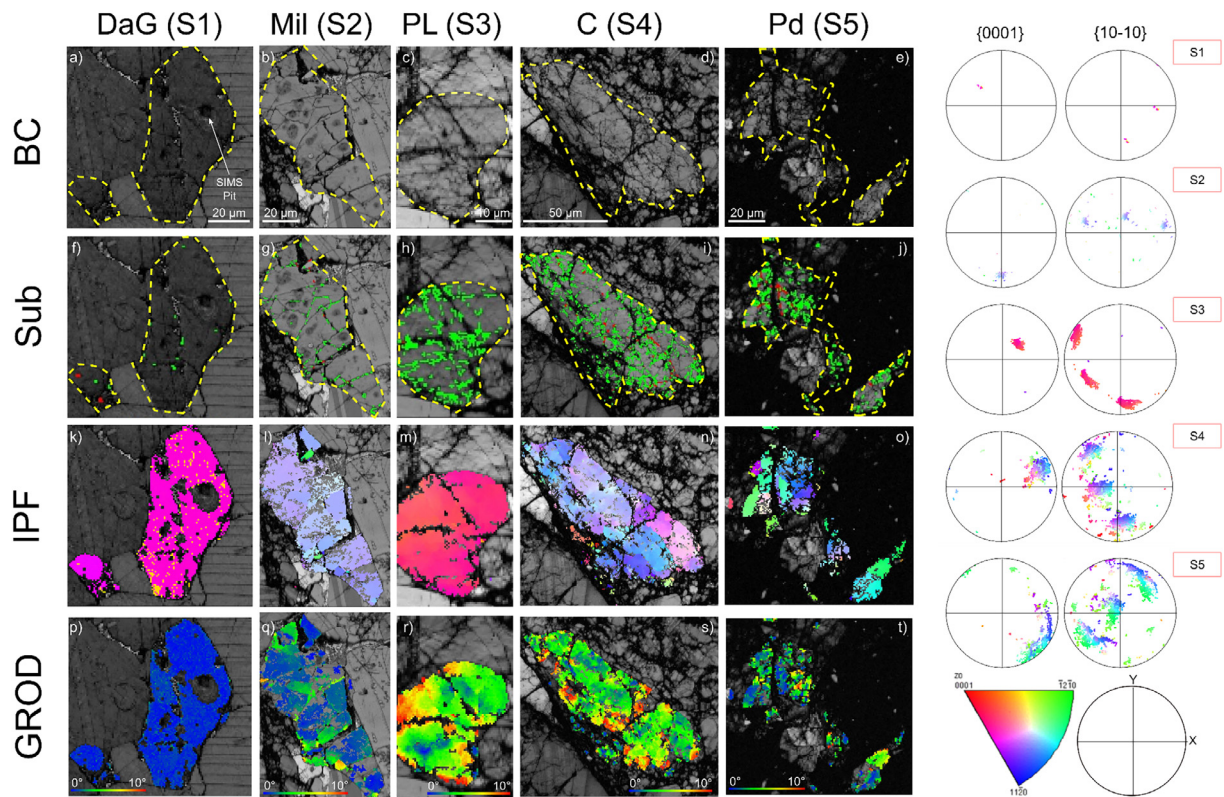

Fig. 2. Representative band contrast (BC), subgrain boundary (SUB), inverse pole figures (IPF), and grain reference orientation deviation (GROD) maps of apatite grains that have experienced deformation from S1 to S5. DaG - DaG 945 (S1), Mil - Millbillillie (S2), PL - Puero Lápice (S3), C - Cachari (S4), Pd - Padvarninkai (S5). The right panel shows upper hemisphere equal area projection pole figures corresponding to the IPF maps. Yellow dashed lines in BC and SUB panels outline the studied apatite grains. Low angle sgrain boundaries (green) are defined here by adjacent pixels with a boundary >2° and <10° misorientation angle whilst high angle grain boundaries (red) have misorientation angle >10°; anything <2° is considered 'strain free'. The IPF figures indicate the severity of internal deformation at >S2 and are colour-coded based on the guide in the bottom right corner. Caption images have the same orientation reference as the pole figures. It should be noted that care is required when interpreting BC maps in this fashion given other factors, such as polishing finish, can also affect the BC image. Care was taken, however, to only collect EBSPs of areas that appeared smooth and free of surface polishing cracks.

>2° and <10° misorientation angle; anything <2° is considered 'strain-free'.

4.1.1. Shock Stage S1

Three apatite grains of sample DaG 945 were analysed with EBSD. DaG 945 is considered unshocked based on the sharp optical extinction angle of largely unfractured plagioclase observed in thin section and, therefore, is assigned an S1 shock stage here. As previously reported (Barrett et al., 2016, 2019), apatite in BSE from this sample are small (~10 to 50 μm in the longest direction), subhedral, and usually occur within late stage mesostasis areas and are believed to be primary in nature based on textural observations. Apatite analysed here do not appear to be near any areas of local recrystallisation. These apatite in EBSD occur as single crystals displaying good diffraction in BC maps and no obvious signs of internal deformation (i.e., crystal lattice bending, low angle misorientations or subgrains) in other EBSD images (Fig. 2f). IPF maps and their corresponding pole figures show tight clustering of orientation data, typical of a single crystal with minimal lattice distortion (~3° see S1 PF in Fig. 2). For S1 apatite (Fig. 2p), GROD maps show no resolvable internal misorientations, and thus no lattice strain or subgrain formation.

4.1.2. Shock Stage S2

Seven apatite grains were analysed with EBSD in S2 samples (five from Millbillillie and two from Stannern). Optical microscopy of both samples indicated undulose extinction in plagioclase, therefore, a shock stage of S2 was assigned to these samples. It should be noted, however, that shock pressure can be heterogenous within a meteorite (e.g. Koroteev et al., 2013; Moreau et al., 2018), especially a polymict sample such as Millbillillie (Yamaguchi et al., 1994). In Stannern, the clouding and deformation twining observed in plagioclase can be indicative of relatively low shock pressures (Jaret et al., 2014). Apatite in BSE images from these samples range from ~10 to 100 μm in the longest direction and are typically subhedral to anhedral. At S2, samples show incipient brecciation and fracturing of apatite and the surrounding minerals in BSE images (Fig. 2l, 2q). The fractures form a network of sub-linear features cross-cutting the apatite, with no obvious preferred orientation, with some fractures being wholly contained within the apatite and others continuing into the surrounding mineral phases. These fractures form mechanically broken blocks which are predominately sub-angular to angular in nature with typically low to no relative misorientation between them in EBSD (Fig. 2l and S2 PF). Internally, these blocks typically show a low spread in misorientation (typically up to 3° misorientation) which may indicate minimal crystal-plastic deformation (Fig. 2q). While apatite grains in Stannern potentially display some evidence of early stage subgrain formation (although some of these low angle grain boundaries appear to be related to cracks; see Stannern subgrain boundary maps in the supplementary material), Millbillillie apatite typically do not, only displaying fracturing of the grains (Fig. 2q). BC maps in both samples, excluding one apatite grain in Stannern, display good EBSP quality.

4.1.3. Shock Stage S3 and S4

A total of six apatite grains were analysed with EBSD for Puerto Lápice and three for Cachari. In Puerto Lápice BSE images, apatite are typically ~50 μm in the longest direction (although rarely they can be up to 100 μm), subhedral to anhedral, and mainly in contact with pyroxene, plagioclase and/or a silica phase. Apatite in Cachari are larger (up to 150 μm in the longest direction), also subhedral to anhedral in nature and with similar textures to Puerto Lápice. Cachari apatite are also, generally, heavily fractured compared to Puerto Lápice. In BC maps, S3 and S4 stage apatite are darker and more granular than S1 and S2 shock stages, which could indicate a degradation of the Kikuchi patterns and increasing microstructural complexity (e.g., increasing density of low angle subgrain boundaries) that cannot readily be seen in BSE images (Fig. 2h and i). It should be noted, however, that care is required when interpreting BC maps in this fashion given other factors, such as polishing finish, can also affect the BC image. Nevertheless, care was taken to collect EBSPs only of the areas that appeared smooth and free of surface polishing cracks. Comparing the surface quality of surrounding minerals and their EBSP quality, the drop in signal is only observed in apatite and maskelynite, suggesting that the factors contributing to the EBSP reduction are likely of intrinsic, i.e. structural, nature. Subgrains are also more prevalent in these stages (Fig. 2h and i). This indicates a progressively larger deviation from a strain-free crystal with increasing shock stage. S3 and S4 both show increasing complexity in GROD and IPF maps (as demonstrated by higher levels of misorientation in GROD and greater variation of orientations with a more diverse colour pallet in IPF), with signs of intensive crystal plastic deformation (Fig. 2m and n). IPF maps of Cachari typically contain a larger spread of orientations than the Puerto Lápice, as indicated by a patchier colour scheme. These patches do not appear to follow the main fractures in BSE and BC images except where fractures are particularly large (Figs. 1d and 2d). Internally, these patches also display some degree of spread and local misorientation and subgrain boundary maps support these regions are subgrains (see Cachari supplementary material). The PF for Puerto Lápice (S3) in Fig. 2 indicates, for this particular apatite, that rotation of the apatite *m* plane has occurred around the *c* axis; this may also be observed to a lesser extent in PL-Ap1 (see supplementary material). Pole figures for these samples can show up to ~30° spread in orientations with Cachari showing more extensive rotation than Puerto Lápice and increased density of subgrains which could potentially reflect recrystallisation (Fig. 2 PFs for S3 and S4 and C-Ap3 GROD map in the supplementary material).

4.1.4. Shock Stage S5:

Eight apatite grains in Padvarninkai were analysed with EBSD. At the highest levels of shock deformation (S5), apatite is usually found in direct contact with, or in close proximity to, a diaplectic plagioclase glass and reveals extensive subgrain formation (Fig. 2j) and potentially recrystallisation (as outlined by the fragmental domains in BC maps not observed in BSE). Apatite grains are also associated with

later-forming minerals such as chromite and ilmenite which are considered magmatic in origin. In BSE images, most apatite grains are ~50–100 μm in the longest direction, subhedral to anhedral and are heavily fractured, with some indication of scalloped edges in two grains (Pa-Ap1 and Pa-Ap6; see supplementary material). Two grains (Pa-Ap2 and Pa-Ap3), however, are smaller (~10 μm), show no fracturing and lower spread in crystallographic orientation (~13° and 4°, respectively) relative to the other grains in the sample (up to ~60°), possibly indicative of these grains experiencing lower shock (owing to shielding from other grains) or being completely annealed (see discussion for more details). The spread of orientations observed in pole figures increases with shock, as shown in the pole figures and in the GROD maps. S5 apatite grains display up to ~60° of continuous spread in orientation in their pole figures (Fig. 2, PF S5). There is, however, significant intra-sample variation of crystallographic spread in pole figures, possibly suggesting that some apatite grains have been shielded from shock more effectively than others (Stöffler et al., 1991; Fritz et al., 2017).

Overall the EBSD maps obtained here display progressively larger variations in internal misorientations with increasing shock level in a similar manner to those observed in lunar Apollo 17 samples by Černok et al. (2019).

4.2. Volatile (H and Cl) abundance and isotopic compositions

A total of 19 chlorine measurements on 12 individual apatite grains were made on the three moderate- to high-shock (S3 Puerto Lápice $n = 5$, S4 Cachari $n = 6$, and S5 Padvarninkai $n = 8$) samples and a total of 17 correlated H measurements were made on top of the Cl image pits (Puerto Lápice $n = 5$, Cachari $n = 6$, and Padvarninkai $n = 6$), the data for which are listed in Table 2 and plotted in Figs. 3 and 4. Where possible, within the same apatite grain, one measurement was taken where EBSD maps showed low deviation in crystallographic orientation and another measurement was taken where these maps indicated higher misorientations, to allow for intra-grain comparisons.

Apatite in moderately-shocked Puerto Lápice (S3) display a range in Cl content from ~750 to 1100 ppm with most analyses yielding >900 ppm Cl, similar to the basaltic eucrite NWA 1908 (Sarafian et al., 2017b). Apatite in Cachari (S4) and Padvarninkai (S5) contain more Cl overall, with Cl contents ranging from ~1000 to 1400 ppm; similar to the literature values for Cachari (Sarafian et al., 2017b), Stannern, and DaG 844 (Barrett et al., 2019). The $\delta^{37}Cl$ values for apatite in Puerto Lápice (~–3.4 ± 1.1 to −0.6 ± 1.1‰, 2σ) are within error of terrestrial values (−0.2 ± 1.0‰, Sharp et al., 2013) although typically lower (<−2‰). These values are also similar to the light Cl isotope signature observed in other eucrites (Sarafian et al., 2017b; Barrett et al., 2019) as well as Mars (Williams et al., 2016; Shearer et al., 2018) that are interpreted to record the primitive solar nebula composition. Both Cachari and Padvarninkai have relatively ^{37}Cl-enriched signatures (~+5.4 ± 1.1‰ to ~+7.5 ± 1.2‰ and ~+3.0 ± 1.4‰ to ~+7.7 ± 0.9‰, respectively), similar to some previously analysed basaltic eucrites (Sarafian et al.,

Table 2
Background corrected hydrogen (δD) and chlorine (δ^{37}Cl) isotopic compositions, abundance, and their associated (2σ) uncertainties for apatite in eucrites. Also reported is a weighted average for each sample.

| Sample ID	δD (‰)	2σ (‰)	H$_2$O content (ppm)	2σ (ppm)	δ^{37}Cl (‰)	2σ (‰)	Cl content (ppm)	2σ (ppm)
Cachari								
C-Ap1a	−55	112	285	6	6.63	0.98	1257	35
C-Ap1b	17	86	494	10	5.44	1.09	1016	28
C-Ap2a	58	63	780	16	6.36	1.15	1016	27
C-Ap2b	98	66	738	15	7.49	1.15	1157	24
C-Ap3a	−56	134	186	4	4.92	1.35	1308	28
C-Ap3b	−5	99	325	7	6.98	0.89	1408	30
Weighted Average	**37**	**61**	**286**	**170**	**6.43**	**0.92**	**1182**	**170**
Padvarninkai								
Pa-Ap1a	29	72	614	14	6.19	1.39	1023	31
Pa-Ap1b	-	-	-	-	7.70	0.95	964	29
Pa-Ap2	−157	55	1651	36	3.48	1.23	1391	42
Pa-Ap3	−24	70	646	14	2.96	1.37	1360	41
Pa-Ap4	62	40	3017	68	4.13	1.09	1053	32
Pa-Ap5a	-	-	-	-	5.41	1.04	1208	37
Pa-Ap5b	129	52	1301	29	4.64	1.05	1116	34
Pa-Ap6	114	35	4012	91	4.23	1.22	1193	36
Weighted Average	**50**	**100**	**824**	**600**	**5.10**	**1.3**	**1129**	**120**
Puerto Lápice								
PL-Ap1a	104	103	240	5	−0.65	1.09	940	47
PL-Ap1b	87	65	737	15	−2.12	1.59	754	37
PL-Ap2a	154	58	842	18	−2.02	1.18	983	27
PL-Ap2b	163	58	772	16	−1.22	1.28	1106	31
PL-Ap3	100	69	651	14	−3.38	1.19	959	27
Weighted Average	**128**	**29**	**387**	**320**	**−1.80**	**1.4**	**965**	**140**
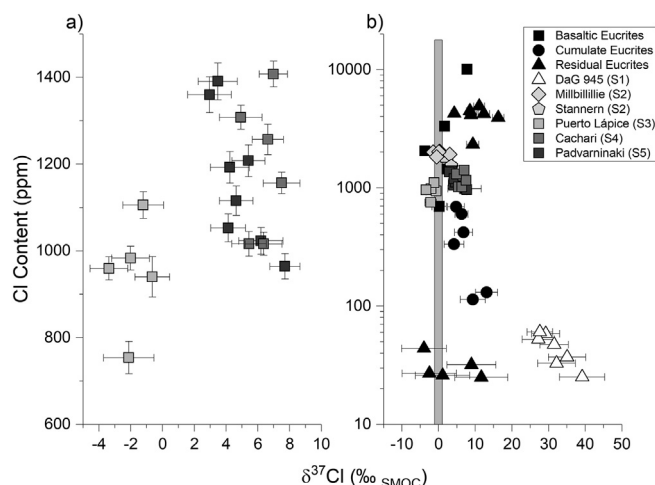
Fig. 3. (a) Plot of Cl content versus $\delta^{37}Cl$ values of apatite in the studied eucrites measured by NanoSIMS. (b) Same data plotted against literature values and averages (Sarafian et al., 2017a,b,c; Barrett et al., 2019). The dark grey band indicates the terrestrial range ($-0.2 \pm 1.0‰$, Sharp et al., 2013). The diagram indicates a consistent Cl isotope composition but varying Cl abundance. When compared to literature values (b) the data from this study plots in consistently with the basaltic eucrites in terms of both Cl content and isotopic composition.
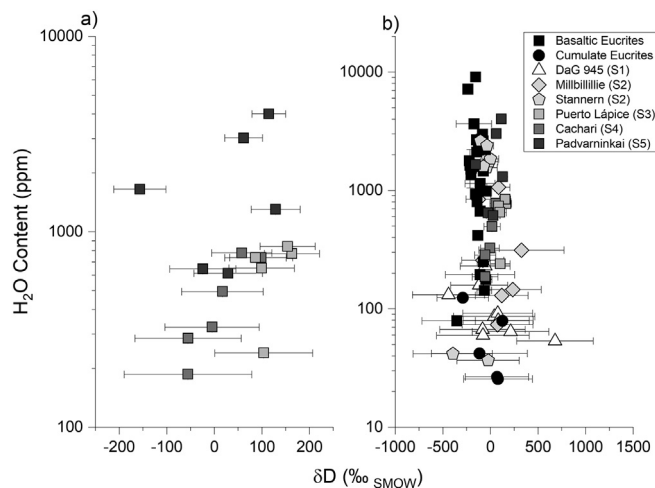

Fig. 4. (a) Plot of H_2O content versus δD values of apatite in the studied eucrites measured by NanoSIMS. (b) Same data plotted against literature values (Sarafian et al., 2014, 2017a,b,c; Barrett et al., 2016). The diagram indicates a consistent H isotope composition but varying H_2O abundance. In Cachari (S4) and Padvarninkai (S5) there appears to be a positive correlation between δD and H_2O content. When compared to literature values (b) the data from this study plots in consistently with the basaltic eucrites in terms of both H_2O content and H isotopic composition.

2017b; Barrett et al., 2019), although Padvarninkai shows slightly more variability (Fig. 3). Data from Puerto Lápice (S3) show similar Cl isotopic compositions and abundances in spot mode to grains that were analysed in isotope imaging mode, which suggests that there is no instrumental effect between these two analysis modes. The weighted average $\delta^{37}Cl$ value of all apatite grains from this study ($+4.0 \pm 1.7‰$; $n = 19$; 95 % confidence) is just within error of the eucrite average ($+1.7 \pm 0.71‰$; Barrett et al., 2019). When combined with the eucrite literature values, the total weighted average of $\delta^{37}Cl$ is $+1.76 \pm 0.66‰$ ($n = 147$; 95 % confidence) which is still within the range of data defined by terrestrial rocks, martian meteorites, and chondritic meteorites ($\delta^{37}Cl \sim -5.6‰$ to $+8.6‰$) (Sharp et al., 2013, 2016; Williams et al., 2016; Bellucci et al., 2017).

Water abundances (reported as equivalent H_2O abundances) for Puerto Lápice (S3) apatite grains exhibit a relatively large variation from 240 to 842 ppm H_2O, similar to the basaltic eucrite Millbillillie (S2) (Fig. 4) (Barrett et al., 2016). Cachari (S4) has a similar range to Puerto Lápice (S3) at 186–780 ppm H_2O (Fig. 4); the highest measured value being ~150 ppm lower than the single data point found in literature (932 ppm; Sarafian et al., 2014). Padvarninkai (S5), on the other hand, has a larger and more variable range in water contents, from 614 to 4012 ppm H_2O (Fig. 4). The δD values of apatite in Puerto Lápice range from $\sim + 90 \pm 65‰$ to $+160 \pm 58‰$ (2σ) within error of many of the basaltic eucrites with similar H_2O abundance. The δD values for some of Cachari ($\sim -55 \pm 135‰$ to $+98 \pm 66‰$) are within error of the previous

data point ($-158 \pm 24‰$; Sarafian et al., 2014), however, apatite display a positive correlation between δD and H_2O content (Fig. 4a). Padvarninkai displays a similar range to Cachari (δD $\sim-157 \pm 55‰$ to $+129 \pm 52‰$), with the lightest single data point from a grain domain with poor BC diffraction. The weighted average δD value of all apatite grains from this study ($+67 \pm 43‰$; $n = 17$; 95 % confidence) is heavier than the literature eucrite average ($-141 \pm 16‰$, data from; Sarafian et al., 2014, 2017a,b,c; Barrett et al., 2016; Stephant et al., 2021). When combined with literature data the total weighted average is $-122 \pm 20‰$ ($n = 85$, 95% confidence) still consistent with D/H values measured in carbonaceous chondrites, terrestrial material and lunar mantle-derived lithologies (e.g. Robert, 2006; Alexander et al., 2012; Hallis et al., 2015; McCubbin and Barnes, 2019).

5. DISCUSSION

5.1. Correlating deformation and volatiles

As mentioned previously in the introduction, the EBSD maps acquired for samples with previous literature data from Barrett et al. (2016, 2019) (DaG 945, Millbillillie, Stannern) are conducted on the exact apatite grains used in those studies. This allows for a valid correlation between the structures observed in this study and the abundance and isotopic composition within these samples. The effects of terrestrial weathering are discussed in the supplementary material.

5.1.1. Shock Stage S1
Pole figures and IPF maps of apatite in DaG 945 show tight clustering in a single orientation ($\sim1°$). Given these grains appear strain-free and without internal features, this sample can be considered practically undeformed. As such neither shock pressure, nor the post-shock elevated temperature, should affect the volatile isotopic composition of the sample. Literature data for the same three apatite grains in DaG 945 (three Cl measurements, three H measurements) which have new EBSD maps (this study) are consistent and invariant with regards to their H isotope systematics and to samples of higher shock stages (Fig. 4b). For chlorine, on the other hand, residual eucrite DaG 945 is an obvious exception in Fig. 3b, with very low Cl content (~30 ppm) and significantly elevated $\delta^{37}Cl$ values ($\sim+30‰$). Given the undeformed nature of the apatite grains as demonstrated by EBSD, and the low-shock stage characteristics of the entire sample, it is unlikely that this enriched ^{37}Cl signature was caused by shock deformation and more likely caused by another secondary mechanism such as degassing as suggested in Barrett et al. (2019).

5.1.2. Shock Stage S2
BSE and EBSD maps of apatite from Millbillillie and Stannern along with the surrounding mineral phases indicate the onset of brecciation and fracturing (Fig. 1b and supplementary material). Results from this work confirm that fracturing is the preferred mode of deformation in samples studied here for this shock stage and suggestive of a dominant brittle deformation regime. The EBSD observations, taking into account the optical properties of minerals, surrounding mineralogy, and textual context, suggest that S2 apatite have experienced relative low pressures (<10 GPa; Fritz et al., 2017). Very high shock-induced pressure can be ruled out based on the absence of pervasive crystal-plastic deformation (dislocation glide, or dislocation creep if high pressure was coupled with sufficient temperature) observed in the apatite (Nakano et al., 2001; Saka et al., 2008). Fritz et al. (2017) postulate a post-shock temperature range of 20–50 °C for samples in the S2 category effectively ruling out dislocation creep and dynamic recrystallisation. Given the slow diffusion of volatiles in apatite at temperatures <200 °C (Brenan, 1993) it is unlikely that the slightly elevated post-shock temperatures would have allowed for diffusion in S2 apatite, even if fracturing could have provided pathways for volatile migration.

Literature data for same eight apatite grains in Millbillillie and Stannern (eight Cl measurements, 11H measurements) which have new EBSD maps (this study), do not appear related to the deformation features observed with EBSD or record any consistent variation which would suggest volatile mobility caused by fracturing (Sarafian et al., 2014, 2017b; Barrett et al., 2016, 2019). Both fractured and unfractured apatite within these samples have uniform $\delta^{37}Cl$ values and Cl contents. These values are also consistent with the majority of basaltic eucrite literature data (typically S2) which display a range from $\sim-$ 1‰ to $+ 3‰$, close to terrestrial values (Sarafian et al., 2017b; Barrett et al., 2019). The Cl content of these samples are also fairly consistent both in terms of intra-grain and inter-grain variations within a sample (Fig. 3b) (Millbillillie: ~1830–2010 ppm Cl, Stannern: 1490–1537 ppm Cl; Barrett et al., 2019). Low temperature mechanical fracturing, the most prevalent textural feature observed in these low shock samples, therefore, does not appear to have provided pathways for volatile migration within these samples.

Neither mineral fracturing, nor the presence of local misorientations seem to affect the abundance or isotopic composition of H in these samples. As each apatite grain appears to be a single crystal, based on BSE and EBSD images (Figs. 1 and 2 and supplementary material), with fragments predominately produced by mechanical fracturing at relatively low temperatures, shock cannot explain any intra-grain variation of H_2O seen within the same apatite either. Stannern and Millbillillie contain apatite with both high and low H_2O contents (59–2624 ppm and 91–1080 ppm H_2O respectively; Sarafian et al., 2014; Barrett et al., 2016) and would, therefore, suggest that H2O content is unlikely to be linked to shock-stage as isotopic fractionation would be expected if volatile mobilisation had occurred and the isotopic composition of the samples are consistent across the full range of H2O content as well as consistent with other eucrites of differing shock stages. One grain in Millbillillie (Ap1, Table 2, Barrett et al., 2016) displays a range of almost 600 ppm H_2O, however, pole figures and GROD maps for this grain show no significant evidence of crystal plastic deformation, and the SIMS pits are not located in areas of higher or lower deformation (See supplementary material). It is, therefore, based on the

textural context and mineral setting with other primary minerals, likely that this variation is primary in nature in agreement with earlier conclusions (Barrett et al., 2016). Overall, The H isotope signature and water content of these samples appears invariant with respect to shock.

5.1.3. Shock Stage S3 and S4

At shock stages S3 and S4, samples begin to show intense crystal plastic deformation (tens of degrees) in the form of lattice bending and subgrain formation. As mentioned in the results, pole figures for both Puerto Lápice and Cachari display an increase in the spread of orientations (∼30° spread in internal crystallographic misorientations). In Puerto Lápice, pole figures appear to display less random orientations when compared to Cachari, which typically has a larger variation and scatter in pole figure orientation. This increase in internal misorientation is likely related to the increase in shock pressure and temperature and continued denigration of the original apatite crystal structure. The increased pseudo-brittle fracturing observed within the S4 Cachari could be related to loss of mineral cohesion owing to mechanical failure at high strain rates, which agrees with features such as lattice bending observed in IPF and pole figures within the sample that indicate a more crystal-plastic regime for deformation (Fig. 2n and S4 pole figure). Given the lack of melt veins present in this section, the post-shock temperatures experienced by Puerto Lápice (S3) are likely to be low (estimated 100–150 °C; Fritz et al., 2017) and too low to allow for shock-induced diffusion of volatiles in apatite (Brenan, 1993). In Cachari (S4), however, post-shock temperatures across the whole sample (likely 200–300 °C) are above those modelled by Brenan (1993) where no volatile diffusion would occur but likely below the temperatures modelled for rapid H diffusion (500–700 °C; Higashi et al., 2017). As shock pressure can be distributed heterogeneously throughout a sample, however, local temperatures could have been much higher, especially in regions around melt veins (Koroteev et al., 2013; Moreau et al., 2018) (please note that no melt veins are observed in either sample close to the apatite analysed in this study). Given the similarity in both H_2O and Cl abundance and isotopic composition for Cachari with lower shock literature values which have not experienced shock-induced diffusion (Sarafian et al., 2014, 2017a,b,c; Barrett et al., 2016, 2019), it is likely that the volatile composition of Cachari is primary and unmodified by post-shock heating.

For S3 sample Puerto Lápice, there is no resolvable intra-grain variation with regards to $\delta^{37}Cl$ values that can be related to obvious subgrains within a single crystal (Fig. 5b). The Cl contents of this sample, however, could potentially have been affected by shock, as in two grains the more deformed areas contain less Cl (∼120–200 ppm) relative to the less deformed areas, and have lower (although within error) $\delta^{37}Cl$ values (see PL-Ap1 and PL-Ap2, Fig. 5b). This is consistent with devolatilisation observed in more heavily shocked martian meteorites such as NWA 7755 (Howarth et al., 2015; Wang et al., 2017). It should be noted, however, that the deformation observed in apatite within Puerto Lápice has not experienced as high shock

pressure as NWA 7755 and is relatively consistent, as indicated by similar levels of GROD misorientation and spread in PFs as well as little difference in GROD misorientation within a grain between the regions of higher and lower deformation. As such, shock may not cause this relatively small variation in Cl content within a grain. This subtle trend of lower Cl content in areas of higher GROD misorientation, however, is not so obvious in Cachari. Whilst C-Ap2 and C-Ap3 follow this trend, the more deformed area in C-Ap1 is not consistent with a slightly higher $\delta^{37}Cl$ value (again within error) and ∼200 ppm more Cl than its less deformed counterpart (Fig. 5b).

In Puerto Lápice (S3), the H isotopic composition is consistent (weighted average $\delta D + 128 \pm 29‰$, Table 2, Fig. 4a). The water abundance is also mostly consistent (651–842 ppm H_2O), with only one of the five analyses significantly different (PL-Ap1a at 240 ppm H_2O) (Fig. 5a). The EBSD maps for this grain show little difference in GROD misorientation between the analysis regions (∼2° misorientation) and no obvious features which suggest there is localised deformation that could have provided a pathway for H_2O loss. Whilst there is no resolvable difference in H isotopic composition for Cachari (S4), the analyses corresponding to more deformed regions (higher misorientation in GROD maps) within each grain are isotopically lighter (although still within error), and two of the three grains (C-Ap1 and C-Ap3) also contain less water (by ∼150–200 ppm H_2O) than their less deformed counterparts (Fig. 5a).

5.1.4. Shock Stage S5

Overall, at shock stage S5, most apatite grains are significantly fractured, with an abundance of distinct subgrains (Fig. 2j and supplementary material). Two grains (Pa-Ap3 and Pa-Ap5) do not display these features but their EBSD maps do indicate at least moderate deformation. Given the small size and lower spread in crystallographic orientation observed in EBSD maps for these two grains, it is possible these crystals may have recovered via annealing (recrystallised). Another possibility is the surrounding minerals (typically maskelynite, pyroxene, and the silica phase) effectively shielded the small grains from the extreme shock pressure as local density contrasts between phases of differing shock impedance at smaller scales is more complex and can induce locally heterogenous responses (e.g. Koroteev et al., 2013; Moreau et al., 2018). These grains, therefore, are less shocked than the larger apatite grains in the same sample. Given these grains are still moderately deformed (particularly Pa-Ap3 in GROD) it is more likely that these grains have been shielded than recrystallised.

In the two Padvarninkai apatite where intra-grain comparisons are possible, analyses in Pa-Ap1 are within error for $\delta^{37}Cl$ value and comparable in Cl content (Fig. 5b). In apatite Pa-Ap5 the analysis region that displays higher GROD misorientation, is slightly enriched (still within error) in ^{37}Cl ($+5.41 \pm 1.04‰$ compared to $+4.64 \pm 1.05‰$) but has a slightly higher Cl content (1208 ± 37 vs. 1116 ± 34 ppm Cl), the opposite to that observed in Puerto Lápice (Fig. 5b). Both apatite grains have $\delta^{37}Cl$ values and Cl contents similar to basaltic eucrite literature
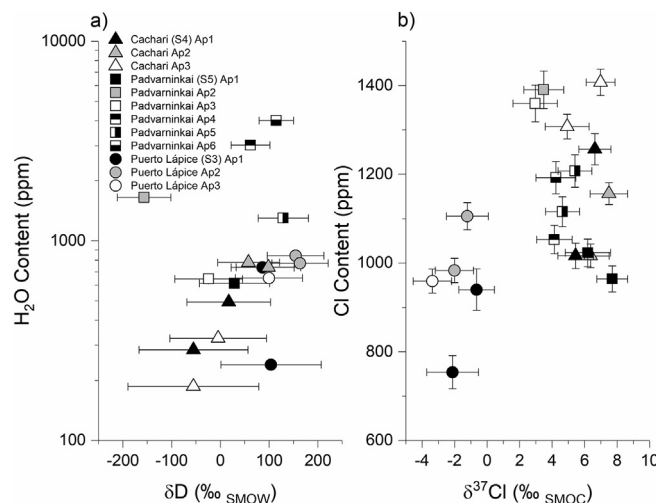
Fig. 5. (a) Plot of intra-grain variability of studied samples for H_2O content and δD values measured by NanoSIMS. (b) Plot of intra-grain variability of studied samples for Cl content and $\delta^{37}Cl$ values. The diagram highlights that there is no resolvable intra-grain variability for both isotope systems, however, there is some intra-grain variability in volatile content. This intra-grain variability of volatile content does not appear to be correlated with analysed conducted in more or less deformed regions of the apatite grain.

data (e.g. NWA 1908; Sarafian et al., 2017b). In both grains which could have undergone recrystallisation, the Cl content and isotopic composition (Pa-Ap3 and Pa-Ap5) are also consistent not only with the rest of the Padvarninkai apatite, but also the lower shock basaltic eucrite literature data (Sarafian et al., 2017b; Barrett et al., 2019).

At the highest shock stage in this study, Padvarninkai (S5) is significantly more variable in both H isotopic composition and content. Unfortunately, owing to the extremely fractured nature of the apatite grains within the sample, it was not possible to obtain multiple hydrogen isotope analyses within a single apatite and therefore no intra-grain comparisons can be made. The lightest H isotope composition in this sample (Pa-Ap2; $-157 \pm 55‰$), is located in a region that in BC images appears to be particularly complex and could represent severely degraded crystallinity despite the low spread in IPF and Pole Figure orientation. This region could act as a 'nano-sponge' for a D-poor reservoir which has been interpreted in water-poor apatite with complex nanostructures on the Moon incorporating a measurable amount of solar hydrogen (Černok et al., 2020). In the case of this sample, however, the H_2O content of this Pa-Ap2 is significantly higher (approximately an order of magnitude) than the lunar case and Pa-Ap5 is also located in a similar region within its apatite crystal and has a more positive δD value ($+62 \pm 40‰$) which suggests there is no consistent link. The H_2O abundance of Pa-Ap2 is also lower than that of Pa-Ap5 (1651 ppm and 3017 ppm H_2O respectively). If these regions did act as a nano-sponge for D-poor water, it would be expected that the higher water content apatite have the lower δD value which is not the case here. Given the strongly hydrophilic nature of Cl, it would be expected that a similar trend be observed in the Cl isotope values; whilst the $\delta^{37}Cl$ value for Pa-Ap2 is low for the sample it is not anomalously low nor the lowest value from the sample and also displays a consistent Cl content. It is, therefore,

unlikely that the complexity observed in BC images is related to isotopic composition. The GROD and local misorientation maps for the rest of this sample, however, do not display any obvious relationship between deformation, δD, and H_2O content (See supplementary material). At this shock stage the post-shock heating (estimated 600–900 °C; Fritz et al., 2017) would have been high enough for diffusion of H through the apatite crystal, however, this heating would be very short lived ($\sim$70 ms, Ozawa et al., 2014) and therefore the distance diffused would be minimal ($\sim$1.5 nm assuming 700 °C for 70 ms using the equation from Higashi et al., 2017 or significantly less using Brenan, 1993). The lack of observed correlation between shock, δD, and H_2O content, owing to the consistent values between high with low shock samples, suggests that diffusion was either 1) not extensive, 2) that the post-shock elevated temperature did not last long enough for volatile diffusion, or 3) given the variable deformation seen across the sample, the post-shock heating for these apatite grains was lower than the estimated temperature from the shock classification, therefore reducing the effectiveness of diffusion.

Whilst there does not appear to be a relationship between deformation features, δD and H_2O content, Fig. 4a does potentially highlight a slight positive correlation between δD and H_2O in both Padvarninkai and Cachari. This positive correlation effectively rules out degassing and diffusion (which would both be negatively correlated) but could potentially arise from mixing with a D-poor, H_2O-poor reservoir in a similar fashion to that observed in Černok et al. (2020). In their case, however, the addition of a D-poor reservoir, was only noted in the driest apatite grains (<100 ppm) all of which were in direct contact with, or in close proximity to, impact generated melt. Apatite with higher water content (>100 ppm) from this study showed no evidence of water loss or alteration in their δD, regardless of the complexity of their

shock-induced features (e.g., spread of misorientations as evidenced in pole figures, density of subgrains). As all the apatite from both Cachari and Padvarninkai contain >100 ppm H_2O and are not located near impact melt, it is unlikely the same process occurred in these samples to any significant degree. This positive correlation is not seen in chlorine isotope systematics, further highlighting the decoupled nature of these two isotope systems in eucrites (Barrett et al., 2019).

Overall, given the consistent results in abundance and isotopic composition of volatiles despite increasing shock pressure and temperature, these results would suggest that there is no systematic and preferential change in Cl or H systematics recorded in apatite as a result of either shock deformation or post-shock heating in the studied samples.

5.2. Thermal metamorphism

Another possible mechanism for altering the primary volatile signature of the eucrites is general thermal metamorphism on the parent body unrelated to short lived elevated post-impact temperatures.

Yamaguchi et al. (1996) suggest a relatively short time scale (~1 Ma) of elevated temperature (~700–900 °C) for global metamorphism on Vesta. Given these parameters and the rapid diffusion of H, parallel of the c axis, in apatite at these temperatures (Higashi et al., 2017) it is possible for H to diffuse well over the distance of the typical size of an apatite grain (~3 cm assuming 700 °C for 1 Ma using the equation from Higashi et al. (2017) or significantly less when considering OH diffusion using Brenan (1993). Diffusion of H in apatite, however, should display a negative correlation of increasing δD and decreasing H_2O content, which is clearly not observed in the results of this study. As there is no evidence for metasomatic alteration within the sample, diffusion of volatiles into the apatite grain has not been considered. Apatite δD and H_2O content of samples studied here do not show any correlation to the

samples overall thermal metamorphic grade (type 4–6), in keeping with pervious apatite literature findings (Sarafian et al., 2014; Barrett et al., 2016) as well as work conducted on clinopyroxene by Sarafian et al. (2019). This is in contrast with the work of Stephant et al. (2021) which indicates a potential link between clinopyroxene H_2O content, δD, and thermal metamorphism. It should be noted, however, the average clinopyroxene data for samples from Stephant et al. (2021) are similar within error and that phosphate data (both apatite and whitlockite) from Stephant et al. (2021) do not show this trend and display H_2O contents and δD values typical for eucrites.

Given the diffusion coefficient of Cl is essentially identical to OH owing to the requirement of charge neutrality (Brenan, 1993), the same negative correlation between $\delta^{37}Cl$ and Cl content would be expected given that ^{35}Cl will diffuse faster than ^{37}Cl and no metasomatism is observed to suggest diffusion into the apatite. This correlation is not observed in the results of this study nor the literature data since apatite from type 4 and 6 eucrites are observed across the entire range of Cl content (Sarafian et al., 2017b; Barrett et al., 2019). In the case of the residual eucrite DaG 945, which has experienced a short period of extreme thermal metamorphism resulting in low level partial melting, Barrett et al. (2019) argue against diffusion or partial melting fractionating Cl isotopes based on recent Cl diffusion work (Fortin et al., 2017).

5.3. Correlating δD and $\delta^{37}Cl$

Fig. 6a displays the correlated δD and $\delta^{37}Cl$ values for regions where it was possible to obtain both sets of isotopic data. Given the hydrophilic nature of Cl, it is possible that there may be a correlation between δD and $\delta^{37}Cl$ values in apatite. From the graph, however, it is obvious that there is no correlation between δD and $\delta^{37}Cl$ values across different samples ($R^2 = 0.10$). Whilst Puerto Lapice (S3 shock) has a resolvable lighter Cl isotopic composition than Cachari and
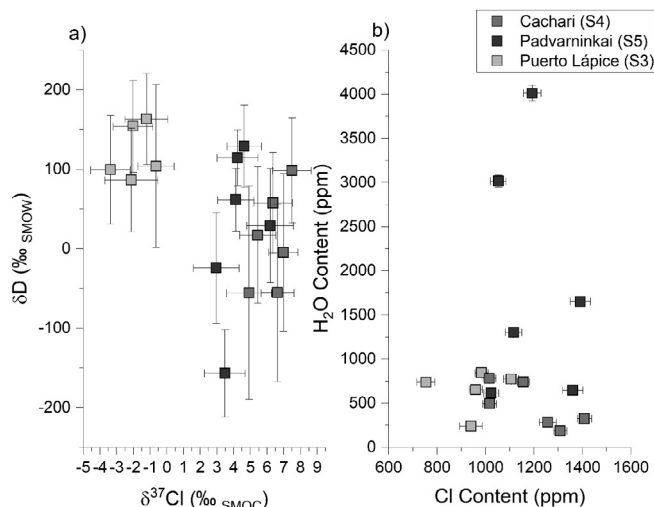

Fig. 6. Plot of correlated δD and $\delta^{37}Cl$ values measured by NanoSIMS for apatite regions where it was possible to obtain both sets of isotopic data. Data presented here indicates there is no correlation between the two isotope systems.
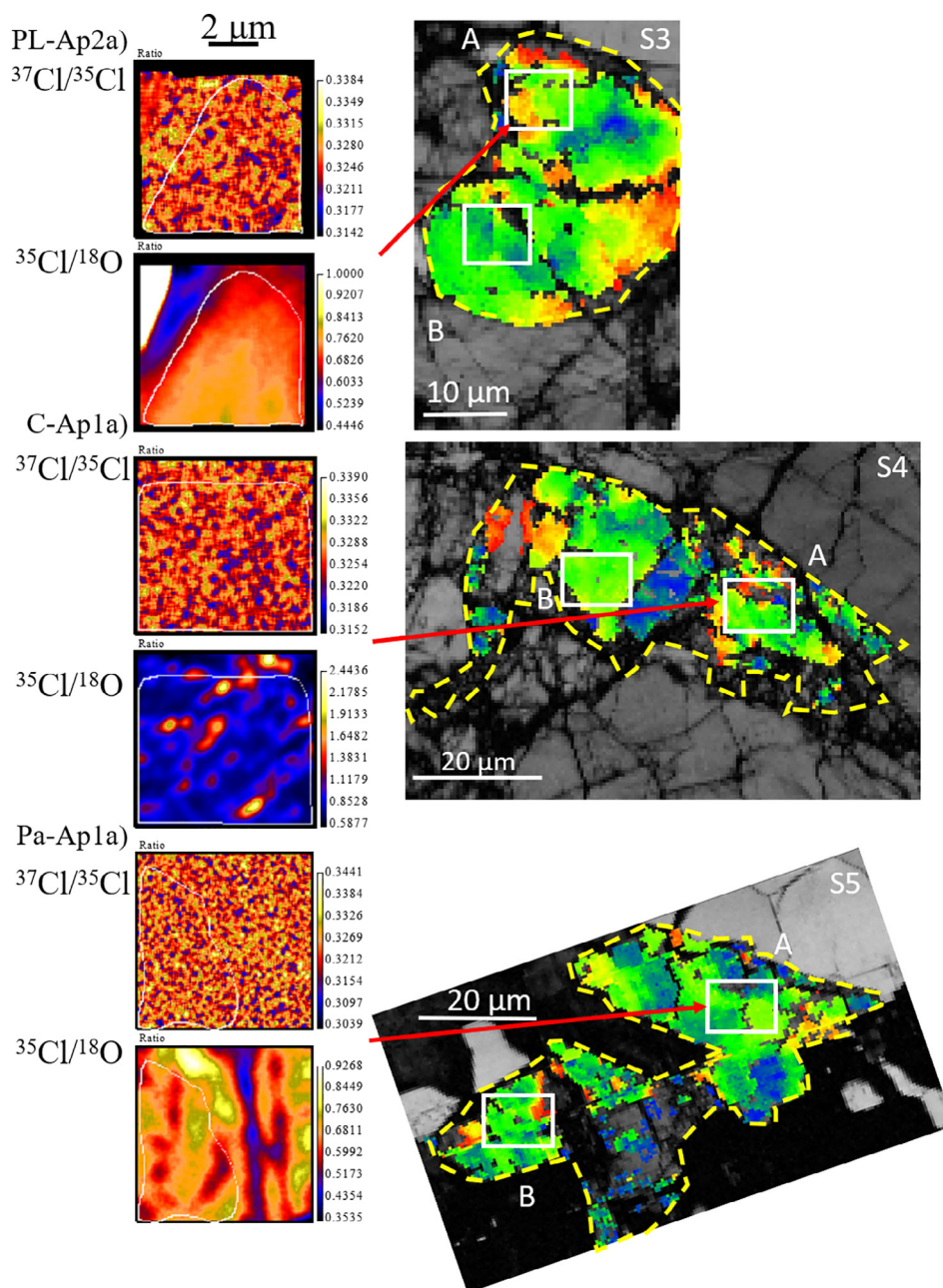
Fig. 7. GROD maps and associated $^{37}Cl/^{35}Cl$ and $^{35}Cl/^{18}O$ images for PL-Ap2a, C-Ap1a, and Pa-Ap1a and are related specifically to the A white box within the GROD map of the figure and indicated by red arrows. The B white box indicates the location of the other analysis within the same grain. White outlines on the $^{37}Cl/^{35}Cl$ and $^{35}Cl/^{18}O$ images indicate the region of interest (ROI) that was used in the study.

Padvaninkai (S4 and S5 shock, respectively), the H isotope systematics are invariant as they are within error at the 2σ level. At S4/S5 shock stages the δD values are more variable, while the δ^{37}Cl values are still consistent. The volatile abundance also exhibits no correlation between H_2O and Cl (Fig. 6b). Even in Padvarninkai, which has a large range in H_2O abundance (~610–4010 ppm), its Cl contents are relatively restricted (~950–1200 ppm; Fig. 6b).

The above results appear contrary to studies of martian phosphates which have been observed to undergo devolatilisation during impact (Howarth et al., 2015), or have

undergone shock-induced phase transitions (Adcock et al., 2017; Wang et al., 2017). Devolatilisation of apatite in enriched shergottite NWA 7755 appears to be associated with impact melt, with the sample containing extensive melt indicative of high post-shock temperatures which could be driving the disturbances observed (Howarth et al., 2015; Wang et al., 2017). Conversely, Hallis et al. (2017) observed that ringwoodite in the martian meteorite Tissint incorporated the D-heavy martian atmosphere during the shock-induced phase transition resulting in higher water content and considerably higher δD values. If devolatilisation
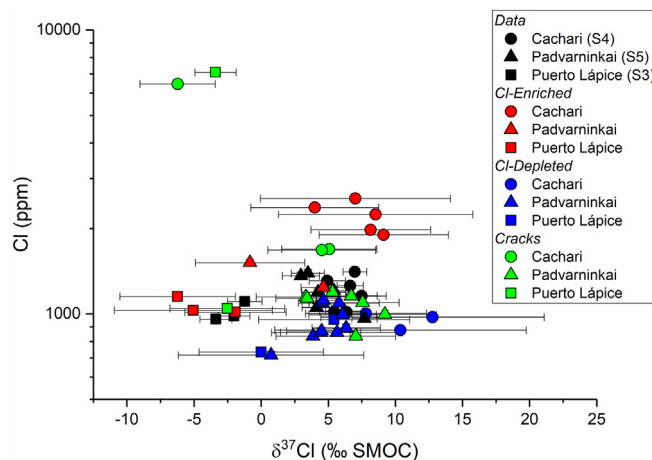
Fig. 8. Plot of Cl content versus $\delta^{37}Cl$ values highlighting the variation in Cl content but not isotopic composition of Cl-enriched and Cl-depleted regions of interest (ROI). Obvious cracks were also added for comparison purposes.

during impact was the mechanism involved in creating the volatile abundance variation observed in our samples, it could also be expected there would be potential isotopic fractionation. Given there is no correlation between the abundance and isotopic composition of either volatile system with shock and little to no melting observed within the samples, devolatilisation cannot be used to explain the variations observed in volatile abundance.

Results of this study, however, are consistent with the recent work of Černok et al. (2020) on lunar samples which demonstrated no evidence of water-loss or alteration of δD in apatite, at appreciable water contents (>100 ppm H_2O), regardless of the complexity of observed shock-induced nanostructures. Combined, these results may indicate a difference in response to shock based on the presence/absence of an atmosphere.

5.4. Nanoscale mobility of Cl in shocked eucrites

As the chlorine isotopic compositions measured in this study were conducted in isotope imaging mode, it is possible to investigate if there are any subtle changes in the isotopic composition across an image. It is then possible to potentially link any observed changes in the isotope image to shock features in EBSD given these analyses are at similar length scales (175–513 nm and 300–750 nm, respectively). The three GROD maps in Fig. 7 for shocked eucrites are displayed alongside Cl isotope SIMS images for one of their analyses (in all cases NanoSIMS images relate to point A on each grain). The figure indicates that there is resolvable heterogeneity in the $^{35}Cl/^{18}O$ images in all samples and this appears to increase with shock stage. Interestingly, however, other than regions on the images that can be related to fractures (indicated by either extremely high or low $^{35}Cl/^{18}O$ ratios; and identified in GROD maps by non-indexed areas), there does not appear to be an obvious link between the sub-micrometre variations seen in the NanoSIMS images and any of the intra-crystalline deformation features in the EBSD images. In PL-Ap2a a distinct subgrain is observed in the GROD map (Fig. 7) but no variation is seen in the $^{35}Cl/^{18}O$ image.

When regions of interest (ROIs) are taken around the smaller and more complex Cl-enriched/depleted regions within an isotope image, the corresponding $\delta^{37}Cl$ value of this ROI is within error of the larger ROI used for the reported data (Table 2). Given the poor counting statistics associated with these smaller ROIs, their respective uncertainties are large unfortunately precluding any meaningful observations. The Cl content, however, can vary up to several hundred ppm (Fig. 8). It is possible the variation in Cl content is facilitated by shock-induced nanostructures that could have provided pathways for migration of volatiles and, as the isotopic composition remains unchanged within error across the apatite grain, there is no evidence for any preferential mobilisation of ^{35}Cl over ^{37}Cl. The $^{35}Cl/^{18}O$ image of Pa-Ap1a does show an approximately linear Cl-depleted region that coincides with a linear feature of non-indexing pixels in EBSD maps which is an observed crack in the apatite crystal which could be used as pathway for volatile migration. Other cracks, however, both within Padvarninkai as well as the other lower shock samples studied do not display the same correlation, with some cracks having elevated Cl abundances and others no discernible difference in Cl content (Fig. 8). Given, therefore, that these features observed in the $^{35}Cl/^{18}O$ images do not appear to coincide with any observed deformation in EBSD maps, and any relation to cracks in the apatite are inconsistent, their direct relation to shock deformation is ambiguous. Improved precision on the Cl isotopic ratio at this small scale and higher-resolution microstructural analysis (such as atom probe tomography and transmission electron microscopy), would be required to further investigate this relationship, as was recently demonstrated in martian shock-deformed apatite (Darling et al., 2021).

6. SUMMARY AND CONCLUSIONS

This study reports on the shock-induced deformation microstructures and corresponding volatile abundance (H, Cl) and isotopic composition of apatite from basaltic eucrites that display a range of shock-deformation features (S1–S5).

EBSD maps of apatite microstructures display increasing spread in internal misorientation at higher shock stages. At shock stage S1, apatite grains are considered unshocked, with single crystals displaying no obvious signs of internal deformation as indicated by tight clustering in IPF and PF. Apatite in S2 samples are predominately deformed by fracturing which form sub-angular to angular blocks with little to no relative misorientation between or within the blocks. S3 and S4 samples display increasing amounts of crystal plastic deformation and at the higher shock stages (S4/S5) there is potential recrystallisation.

The Cl content of shocked (S3 to S5) apatite ranges from ~940 to 1410 ppm, similar to those from less-shocked basaltic eucrites and the corresponding $\delta^{37}Cl$ values range from −3.38 to +7.70‰. The moderately shocked sample Puerto Lápice (S3) has $\delta^{37}Cl$ values similar to Earth (−3.38 to −0.65‰), whereas the more severely shocked Cachari and Padvarninkai are enriched in ^{37}Cl, similar to the typically lower shock basaltic eucrite literature data (Sarafian et al., 2017b; Barrett et al., 2019). The H_2O abundances are more variable (240 to ~4000 ppm) and appear to show increased variability with increased shock stage, however, the overall range in water content is still within the range previously reported for lower-shock basaltic eucrites (Sarafian et al., 2014; Barrett et al., 2016). The δD values, ranging from –157 to +163‰, are also similar to those known for basaltic eucrites. Weighted averages for both H and Cl isotopic systems (δD −122 ± 20‰, $\delta^{37}Cl$ +1.76 ± 0.66‰) are consistent with other inner Solar System values.

Based on the results presented here, the following conclusions can be drawn:

- EBSD maps of the studied eucrite meteorites display an increase in crystallographic misorientation with shock stage. This increase in misorientation, however, does not appear to correlate with either abundance or isotopic composition at either an inter-grain or intra-grain scale.
- Diffusion occurring as a result of elevated post-impact temperatures is unlikely, owing to 1) the low estimated post-impact temperatures at low shock stages (Fritz et al., 2017; Stöffler et al., 2018), 2) the lack of negative correlation linked to diffusion-driven fractionation, and 3) the abundance and isotopic composition of samples studied here do not show any correlation to the samples overall thermal metamorphic grade.
- Whilst the $^{37}Cl/^{35}Cl$ images of apatite do not appear to display any variation with shock stage, the microstructural complexity (local enrichments and depletions in $^{35}Cl/^{18}O$ ratio) observed within the NanoSIMS $^{35}Cl/^{18}O$ images does increase with shock stage. There does not, however, appear to be an obvious or consistent link between the sub-micron variations seen in the NanoSIMS images and any of the intra-crystalline deformation features in the EBSD images.

Overall, results of this study are similar to the recent work of Černok et al. (2020) on lunar apatite but different compared to the results for martian apatite (Darling et al., 2021). As such, H and Cl loss and isotope perturbations associated with shock seem to be a feature currently unique to celestial bodies with atmospheres and/or more extensive past fluid-rock interactions, i.e. Mars. Given the consistent results in abundance and isotopic composition of volatiles despite increasing shock pressure and temperature, and lack of any consistent correlation observed in intra-grain analysis as well as between $^{35}Cl/^{18}O$ images and EBSD maps, these results would suggest that there is no systematic and preferential loss of Cl or H recorded in apatite as a result of either shock deformation or post-shock heating in the studied eucrite samples. Apatite, therefore, appears to be a robust recorder of primary H and Cl signatures on airless bodies.

Declaration of Competing Interest

The authors declare that they have no known competing financial interests or personal relationships that could have appeared to influence the work reported in this paper.

APPENDIX A. SUPPLEMENTARY DATA

Supplementary data to this article can be found online at https://doi.org/10.1016/j.gca.2021.03.018.

REFERENCES

Adcock C. T., Tschauner O., Hausrath E. M., Udry A., Luo S. N., Cai Y., Ren M., Lanzirotti A., Newville M., Kunz M. and Lin C. (2017) Shock-transformation of whitlockite to merrillite and the implications for meteoritic phosphate. *Nat. Commun.* **8**, 14667.

Alexander C. M. O. D., Bowden R., Fogel M. L., Howard K. T., Herd C. D. K. and Nittler L. R. (2012) The provenances of asteroids, and their contributions to the volatile inventories of the terrestrial planets. *Science* **337**, 721–723.

Alexander C. M. O. D., Greenwood R. C., Bowden R., Gibson J. M., Howard K. T. and Franchi I. A. (2018) A mutli-technique search for the most primitive CO chondrites. *Geochim. Cosmochim. Acta* **221**, 406–420.

Barnes J. J., Franchi I. A., Anand M., Tartèse R., Starkey N. A., Koike M., Sano Y. and Russell S. S. (2013) Accurate and precise measurements of the D/H ratio and hydroxyl content in lunar apatites using NanoSIMS. *Chem. Geol.* **337–338**, 48–55.

Barnes J. J., Tartèse R., Anand M., McCubbin F. M., Franchi I. A., Starkey N. A. and Russell S. S. (2014) The origin of water in

the primitive Moon as revealed by the lunar highlands samples. *Earth Planet. Sci. Lett.* **390**, 244–252.

Barnes J. J., Tartèse R., Anand M., McCubbin F. M., Neal C. R. and Franchi I. A. (2016) Early degassing of lunar urKREEP by crust-breaching impact(s). *Earth Planet. Sci. Lett.* **447**, 84–94.

Barrat J.-A., Blichert-Toft J., Gillet P. and Keller F. (2000) The differentiation of eucrites: the role of in situ crystallization. *Meteorit. Planet. Sci.* **35**, 1087–1100.

Barrat J.-A. (2004) Determination of parental magmas of HED cumulates: The effects of interstitial melts. *Meteorit. Planet. Sci.* **39**, 1767–1779.

Barrat J.-A., Yamaguchi A., Greenwood R., Bohn M., Cotten J., Benoit M. and Franchi I. (2007) The Stannern trend eucrites: contamination of main group eucritic magmas by crustal partial melts. *Geochim. Cosmochim. Acta* **71**, 4108–4124.

Barrett T. J., Barnes J. J., Tartèse R., Anand M., Franchi I. A., Greenwood R. C., Charlier B. L. A. and Grady M. M. (2016) The abundance and isotopic composition of water in eucrites. *Meteorit. Planet. Sci.* **51**, 1110–1124.

Barrett T. J., Barnes J. J., Anand M., Franchi I. A., Greenwood R. C., Charlier B. L. A., Zhao X., Moynier F. and Grady M. M. (2019) Investigating magmatic processes in the early Solar System using the Cl isotopic systematics of eucrites. *Geochim. Cosmochim. Acta* **266**, 582–597.

Bellucci J. J., Whitehouse M. J., John T., Nemchin A. A., Snape J. F., Bland P. A. and Benedix G. K. (2017) Halogen and Cl isotopic systematics in Martian phosphates: Implications for the Cl cycle and surface halogen reservoirs on Mars. *Earth Planet. Sci. Lett.* **458**, 192–202.

Binns R. A. (1967) Stony meteorites bearing maskelynite. *Nature* **213**, 1111.

Bischoff A. and Stöffler D. (1992) Shock metamorphism as a fundamental process in the evolution of planetary bodies: information from meteorites. *Eur. J. Mineral.* **4**, 707–755.

Bobe K., Bischoff A. and Stöffler D. (1989) Impact and thermal metamorphism as fundamental processes in the evolution of Stannern, Juvinas, Jonzac, Peramiho, and Millbillillie eucrite parent body (abstract). *Meteoritics* **24**, 252.

Bogard D. D., Taylor G. J., Keil K., Smith M. R. and Schmitt R. A. (1985) Impact melting of the Cachari eucrite 3.0 Gy ago. *Geochim. Cosmochim. Acta* **49**, 941–946.

Borthwick V. E. and Piazolo S. (2010) Post-deformational annealing at the subgrain scale: temperature dependent behaviour revealed by in-situ heating experiments on deformed single crystal halite. *J. Struct. Geol.* **32**, 982–996.

Boyce J. W., Treiman A. H., Guan Y., Ma C., Eiler J. M., Gross J., Greenwood J. P. and Stolper E. M. (2015) The chlorine isotope fingerprint of the lunar magma ocean. *Sci. Adv.* **1**.

Brenan J. M. (1993) Kinetics of fluorine, chlorine and hydroxyl exchange in fluorapatite. *Chem. Geol.* **110**, 195–210.

Bukovanská M., Ireland T. and Janicke J. (1997) Zircons and baddeleyites from differentiated meteorites—basaltic achondrites: ion probe dating and REE systematics. *J. Geosci.* **42**, 20.

Černok A., White L. F., Darling J., Dunlop J. and Anand M. (2019) Shock-induced microtextures in lunar apatite and merrillite. *Meteoritics & Planet. Sci.* **54**, 1262–1282.

Černok A., Anand M., Zhao X., Darling J. R., White L. F., Stephant A., Dunlop J., Tait K. T. and Franchi I. A. (2020) Preservation of primordial signatures of water in highly-shocked ancient lunar rocks. *Earth Planet. Sci. Lett.* **544** 116364.

Cox M. A., Erickson T. M., Schmieder M., Christoffersen R., Ross D. K., Cavosie A. J., Bland P. A., Kring D. A. and Scientists I. I. E. (2020) High-resolution microstructural and compositional analyses of shock deformed apatite from the peak ring of the Chicxulub impact crater. *Meteoritics & Planet. Sci.* **55**.

Daly L., Piazolo S., Lee M. R., Griffin S., Chung P., Campanale F., Cohen B. E., Hallis L. J., Trimby P. W., Baumgartner R., Forman L. V. and Benedix G. K. (2019) Understanding the emplacement of Martian volcanic rocks using petrofabrics of the nakhlite meteorites. *Earth Planet. Sci. Lett.* **520**, 220–230.

Darling J. R., Moser D. E., Barker I. R., Tait K. T., Chamberlain K. R., Schmitt A. K. and Hyde B. C. (2016) Variable microstructural response of baddeleyite to shock metamorphism in young basaltic shergottite NWA 5298 and improved U-Pb dating of Solar System events. *Earth Planet. Sci. Lett.* **444**, 1–12.

Darling J. R., White L. F., Kizovski T., Černok A., Moser D. E., Tait K. T., Dunlop J., Langelier B., Douglas J. O., Zhao X., Franchi I. A. and Anand M. (2021) The shocking state of apatite and merrillite in shergottite Northwest Africa 5298 and extreme nanoscale chlorine isotope variability revealed by atom probe tomography. *Geochim. Cosmochim. Acta* **293**, 422–437.

Eugster O. and Michel T. (1995) Common asteroid break-up events of eucrites, diogenites, and howardites and cosmic-ray production rates for noble gases in achondrites. *Geochim. Cosmochim. Acta* **59**, 177–199.

Forman L. V., Bland P. A., Timms N. E., Collins G. S., Davison T. M., Ciesla F. J., Benedix G. K., Daly L., Trimby P. W., Yang L. and Ringer S. P. (2016) Hidden secrets of deformation: impact-induced compaction within a CV chondrite. *Earth Planet. Sci. Lett.* **452**, 133–145.

Forman L. V., Bland P. A., Timms N. E., Daly L., Benedix G. K., Trimby P. W., Collins G. S. and Davison T. M. (2017) Defining the mechanism for compaction of the CV chondrite parent body. *Geology* **45**, 559–562.

Fortin M.-A., Watson E. B. and Stern R. (2017) The isotope mass effect on chlorine diffusion in dacite melt, with implications for fractionation during bubble growth. *Earth Planet. Sci. Lett.* **480**, 15–24.

Fredriksson K. and Kraut F. (1967) Impact glass in the Cachari eucrite. *Geochim. Cosmochim. Acta* **31**, 1701–1704.

Fritz J., Greshake A. and Fernandes V. A. (2017) Revising the shock classification of meteorites. *Meteorit. Planet. Sci.* **52**, 1216–1232.

Goldoff B., Webster J. D. and Harlov D. E. (2012) Characterization of fluor-chlorapatites by electron probe microanalysis with a focus on time-dependent intensity variation of halogens. *Am. Mineral.* **97**, 1103–1115.

Greenwood J. P., Itoh S., Sakamoto N., Vicenzi E. P. and Yurimoto H. (2008) Hydrogen isotope evidence for loss of water from Mars through time. *Geophys. Res. Lett.* **35**, L05203.

Greenwood R. C., Franchi I. A., Jambon A. and Buchanan P. C. (2005) Widespread magma oceans on asteroidal bodies in the early solar system. *Nature* **435**, 916–918.

Hagemann R., Nief G. and Roth E. (1970) Absolute isotopic scale for deuterium analysis of natural waters. Absolute D/H ratio for SMOW1. *Tellus* **22**, 712–715.

Hallis L. J., Taylor G. J., Nagashima K. and Huss G. R. (2012a) Magmatic water in the martian meteorite Nakhla. *Earth Planet. Sci. Lett.* **359–360**, 84–92.

Hallis L. J., Taylor G. J., Nagashima K., Huss G. R., Needham A. W., Grady M. M. and Franchi I. A. (2012b) Hydrogen isotope analyses of alteration phases in the nakhlite martian meteorites. *Geochim. Cosmochim. Acta* **97**, 105–119.

Hallis L. J., Huss G. R., Nagashima K., Taylor G. J., Halldórsson S. A., Hilton D. R., Mottl M. J. and Meech K. J. (2015) Evidence for primordial water in Earth's deep mantle. *Science* **350**, 795–797.

Hallis L. J. (2017) D/H ratios of the inner Solar System. *Philos. Trans. R. Soc. A: Math., Phys. Eng. Sci.* **375**.

Hallis L. J., Huss G. R., Nagashima K., Taylor G. J., Stöffler D., Smith C. L. and Lee M. R. (2017) Effects of shock and Martian alteration on Tissint hydrogen isotope ratios and water content. *Geochim. Cosmochim. Acta* **200**, 280–294.

Higashi Y., Itoh S., Hashiguchi M., Sakata S., Hirata T., Watanabe K. and Sakaguchi I. (2017) Hydrogen diffusion in the apatite-water system: fluorapatite parallel to the c-axis. *Geochem. J.* **51**, 115–122.

Hopkins M., Mojzsis S., Bottke W. and Abramov O. (2015) Micrometer-scale U-Pb age domains in eucrite zircons, impact re-setting, and the thermal history of the HED parent body. *Icarus* **245**, 367–378.

Howarth G. H., Pernet-Fisher J. F., Bodnar R. J. and Taylor L. A. (2015) Evidence for the exsolution of Cl-rich fluids in martian magmas: Apatite petrogenesis in the enriched lherzolitic shergottite Northwest Africa 7755. *Geochim. Cosmochim. Acta* **166**, 234–248.

Hu S., Lin Y., Zhang J., Hao J., Feng L., Xu L., Yang W. and Yang J. (2014) NanoSIMS analyses of apatite and melt inclusions in the GRV 020090 Martian meteorite: Hydrogen isotope evidence for recent past underground hydrothermal activity on Mars. *Geochim. Cosmochim. Acta* **140**, 321–333.

Hutchison R. (2004). Meteorites: a petrologic, chemical and isotopic synthesis. Cambridge University Press.

Jaret S. J., Kah L. C. and Harris R. S. (2014) Progressive deformation of feldspar recording low-barometry impact processes, Tenoumer impact structure, Mauritania. *Meteorit. Planet. Sci.* **49**, 1007–1022.

Kaufmann R., Long A., Bentley H. and Davis S. (1984) Natural chlorine isotope variations. *Nature* **309**, 338–340.

Kenny G. G., Karlsson A., Schmieder M., Whitehouse M. J., Nemchin A. A. and Bellucci J. J. (2020) Recrystallization and chemical changes in apatite in response to hypervelocity impact. *Geology* **48**, 19–23.

Koroteev V., Berzin S., Erokhin Y. V., Ivanov K. and Khiller V. (2013). Composition and structure of the Chelyabinsk meteorite, Doklady Earth Sciences. Springer Nature BV, p. 839.

Kumler B. and Day J. M. D. (2021) Trace element variations generated by magmatic and post-crystallization processes in eucrite meteorites. *Geochim. Cosmochim. Acta.* https://doi.org/10.1016/j.gca.2021.03.002.

Llorca J., Casanova I., Trigo-Rodríguez J. M., Madiedo J. M., Roszjar J., Bischoff A., Ott U., Franchi I. A., Greenwood R. C. and Laubenstein M. (2009) The Puerto Lápice eucrite. *Meteorit. Planet. Sci.* **44**, 159–174.

Lugmair G. and Galer S. (1992) Age and isotopic relationships among the angrites Lewis Cliff 86010 and Angra dos Reis. *Geochim. Cosmochim. Acta* **56**, 1673–1694.

Ma C. and Beckett J. R. (2021) Kaitianite, Ti3+2Ti4+O5, a new titanium oxide mineral from Allende. *Meteorit. Planet. Sci.* **56**, 96–107.

Mason B., Jarosewich E. and Nelen J. A. (1979) The pyroxene-plagioclase achondrites. *Smithson. Contrib. Earth Sci.* **22**, 27–45.

Mayne R., McSween H., McCoy T. and Gale A. (2009) Petrology of the unbrecciated eucrites. *Geochim. Cosmochim. Acta* **73**, 794–819.

McCubbin F. M., Hauri E. H., Elardo S. M., Vander Kaaden K. E., Wang J. and Shearer C. K. (2012) Hydrous melting of the martian mantle produced both depleted and enriched shergottites. *Geology* **40**, 683–686.

McCubbin F. M. and Barnes J. J. (2019) Origin and abundances of H2O in the terrestrial planets, Moon, and asteroids. *Earth Planet. Sci. Lett.* **526** 115771.

McSween H. Y., Binzel R. P., De Sanctis M. C., Ammannito E., Prettyman T. H., Beck A. W., Reddy V., Le Corre L., Gaffey M. J., McCord T. B., Raymond C. A., Russell C. T. and T. the Dawn Science (2013) Dawn; the Vesta–HED connection; and the geologic context for eucrites, diogenites, and howardites. *Meteorit. Planet. Sci.* **48**, 2090–2104.

McSween H. Y., Raymond C. A., Stolper E. M., Mittlefehldt D. W., Baker M. B., Lunning N. G., Beck A. W. and Hahn T. M. (2019) Differentiation and magmatic history of Vesta: constraints from HED meteorites and Dawn spacecraft data. *Geochemistry* **79** 125526.

Merlivat L., Lelu M., Nief G. and Roth E. (1976) Spallation deuterium in rock 70215. In *Lunar and Planetary Science Conference Proceedings*, pp. 649–658.

Misawa K., Yamaguchi A. and Kaiden H. (2005) U-Pb and 207-Pb-206Pb ages of zircons from basaltic eucrites: implications for early basaltic volcanism on the eucrite parent body. *Geochim. Cosmochim. Acta* **69**, 5847–5861.

Mittlefehldt D. W. and Lindstrom M. M. (2003) Geochemistry of eucrites: genesis of basaltic eucrites, and Hf and Ta as petrogenetic indicators for altered Antarctic eucrites. *Geochim. Cosmochim. Acta* **67**, 1911–1934.

Mittlefehldt D. W. (2015) Asteroid (4) Vesta: I. The howardite-eucrite-diogenite (HED) clan of meteorites. *Chem. Erde* **75**, 155–183.

Miura Y., Nagao K., Sugiura N., Fujitani T. and Warren P. (1998) Noble gases, 81Kr-Kr exposure ages and 244Pu-Xe ages of six eucrites, Béréba, Binda, Camel Donga, Juvinas, Millbillillie, and Stannern. *Geochim. Cosmochim. Acta* **62**, 2369–2387.

Moreau J.-G., Kohout T. and Wünnemann K. (2018) Melting efficiency of troilite-iron assemblages in shock-darkening: Insight from numerical modeling. *Phys. Earth Planet. Inter.* **282**, 25–38.

Nakano T., Awazu T. and Umakoshi Y. (2001) Plastic deformation and operative slip system in mineral fluorapatite single crystal. *Scr. Mater.* **44**, 811–815.

Nichols C. I. O., Krakow R., Herrero-Albillos J., Kronast F., Northwood-Smith G. and Harrison R. J. (2018) Microstructural and paleomagnetic insight into the cooling history of the IAB parent body. *Geochim. Cosmochim. Acta* **229**, 1–19.

Ozawa S., Miyahara M., Ohtani E., Koroleva O. N., Ito Y., Litasov K. D. and Pokhilenko N. P. (2014) Jadeite in Chelyabinsk meteorite and the nature of an impact event on its parent body. *Sci. Rep.* **4**, 5033.

Potts N. J., Tartèse R., Anand M., van Westrenen W., Griffiths A. A., Barrett T. J. and Franchi I. A. (2016) Characterization of mesostasis regions in lunar basalts: understanding late-stage melt evolution and its influence on apatite formation. *Meteorit. Planet. Sci.* **51**, 1555–1575.

Prior D. J., Boyle A. P., Brenker F., Cheadle M. C., Day A., Lopez G., Peruzzo L., Potts G. J., Reddy S., Spiess R., Timms Nick E., Trimby P., Wheeler J. and Zetterström L. (999) The application of electron backscatter diffraction and orientation contrast imaging in the SEM to textural problems in rocks. *Am. Mineral.*, 1741.

Prior D. J., Mariani E. and Wheeler J. (2009) EBSD in the earth sciences: applications, common practice, and challenges. In *Electron Backscatter Diffraction in Materials Science* (eds. A. J. Schwartz, M. Kumar, B. L. Adams and D. P. Field). Springer, US, Boston, MA, pp. 345–360.

Robert F. (2006) Solar system deuterium/hydrogen ratio. *Meteorites Early Solar Syst. II* **1**, 341–351.

Roszjar J., Metzler K., Bischoff A., Barrat J.-A., Geisler T., Greenwood R. C., Franchi I. A. and Klemme S. (2011) Thermal history of Northwest Africa 5073—a coarse-grained Stannern-trend eucrite containing cm-sized pyroxenes and large zircon grains. *Meteorit. Planet. Sci.* **46**, 1754–1773.

Saka H., Goto D. and Moon W. J. (2008) Dislocations in plastically deformed apatite. *J. Mater. Sci.* **43**, 3234–3239.

Sarafian A. R., Nielsen S. G., Marschall H. R., McCubbin F. M. and Monteleone B. D. (2014) Early accretion of water in the inner solar system from a carbonaceous chondrite–like source. *Science* **346**, 623–626.

Sarafian A. R., Hauri E. H., McCubbin F. M., Lapen T. J., Berger E. L., Nielsen S. G., Marschall H. R., Gaetani G. A., Righter K. and Sarafian E. (2017a) Early accretion of water and volatile elements to the inner Solar System: evidence from angrites. *Philos. Trans. R. Soc. A: Math., Phys. Eng. Sci.* **375**.

Sarafian A. R., John T., Roszjar J. and Whitehouse M. J. (2017b) Chlorine and hydrogen degassing in Vesta's magma ocean. *Earth Planet. Sci. Lett.* **459**, 311–319.

Sarafian A. R., Nielsen S. G., Marschall H. R., Gaetani G. A., Hauri E. H., Righter K. and Sarafian E. (2017c) Angrite meteorites record the onset and flux of water to the inner solar system. *Geochim. Cosmochim. Acta* **212**, 156–166.

Sarafian A. R., Nielsen S. G., Marschall H. R., Gaetani G. A., Righter K. and Berger E. L. (2019) The water and fluorine content of 4 Vesta. *Geochim. Cosmochim. Acta* **266**, 568–581.

Sharp Z. D., Mercer J. A., Jones R. H., Brearley A. J., Selverstone J., Bekker A. and Stachel T. (2013) The chlorine isotope composition of chondrites and Earth. *Geochim. Cosmochim. Acta* **107**, 189–204.

Sharp Z. D., Williams J. T., Shearer C. K., Agee C. B. and McKeegan K. D. (2016) The chlorine isotope composition of Martian meteorites 2. Implications for the early solar system and the formation of Mars. *Meteorit. Planet. Sci.* **51**, 2111–2126.

Shearer C. K., Messenger S., Sharp Z. D., Burger P. V., Nguyen A. N. and McCubbin F. M. (2018) Distinct Chlorine Isotopic Reservoirs on Mars.: implications for character, extent and relative timing of crustal interaction with mantle-derived magmas, evolution of the martian atmosphere, and the building blocks of an early Mars. *Geochim. Cosmochim. Acta* **234**, 24–36.

Shukolyukov A. and Begemann F. (1996) Cosmogenic and fissiogenic noble gases and 81Kr-Kr exposure age clusters of eucrites. *Meteorit. Planet. Sci.* **31**, 60–72.

Stephant A., Anand M., Zhao X., Chan Q. H. S., Bonifacie M. and Franchi I. A. (2019) The chlorine isotopic composition of the Moon: Insights from melt inclusions. *Earth Planet. Sci. Lett.* **523** 115715.

Stephant A., Wadhwa M., Hervig R., Bose M., Zhao X., Barrett T. J., Anand M. and Franchi I. A. (2021) A deuterium-poor water reservoir in the asteroid 4 Vesta and the inner Solar System. *Geochim. Cosmochim. Acta* **297**, 203–219.

Stöffler D., Keil K. and Edward R. D. S. (1991) Shock metamorphism of ordinary chondrites. *Geochim. Cosmochim. Acta* **55**, 3845–3867.

Stöffler D., Hamann C. and Metzler K. (2018) Shock metamorphism of planetary silicate rocks and sediments: Proposal for an updated classification system. *Meteorit. Planet. Sci.* **53**, 5–49.

Stolper E. (1977) Experimental petrology of eucritic meteorites. *Geochim. Cosmochim. Acta* **41**, 587–611.

Takeda H. and Graham A. (1991) Degree of equilibration of eucritic pyroxenes and thermal metamorphism of the earliest planetary crust. *Meteoritics* **26**, 129–134.

Tartèse R., Anand M., Barnes J. J., Starkey N. A., Franchi I. A. and Sano Y. (2013) The abundance, distribution, and isotopic composition of Hydrogen in the Moon as revealed by basaltic lunar samples: Implications for the volatile inventory of the Moon. *Geochim. Cosmochim. Acta* **122**, 58–74.

Tkalcec B. J., Golabek G. J. and Brenker F. E. (2013) Solid-state plastic deformation in the dynamic interior of a differentiated asteroid. *Nat. Geosci.* **6**, 93–97.

Tkalcec B. J. and Brenker F. E. (2014) Plastic deformation of olivine-rich diogenites and implications for mantle processes on the diogenite parent body. *Meteorit. Planet. Sci.* **49**, 1202–1213.

Tkalcec B. J. and Brenker F. E. (2019) Absence of olivine orientation fabric in highly shocked Martian dunite. *Meteorit. Planet. Sci.* **54**, 267–279.

Touboul M., Sprung P., Aciego S. M., Bourdon B. and Kleine T. (2015) Hf–W chronology of the eucrite parent body. *Geochim. Cosmochim. Acta* **156**, 106–121.

Treiman A. H. (1997) The parent magmas of the cumulate eucrites: a mass balance approach. *Meteorit. Planet. Sci.* **32**, 217–230.

Wang S.-Z., Zhang A.-C., Pang R.-L., Chen J.-N., Gu L.-X. and Wang R.-C. (2017) Petrogenesis and shock metamorphism of the enriched lherzolitic shergottite Northwest Africa 7755. *Meteorit. Planet. Sci.* **52**, 2437–2457.

Wang Y., Hsu W. and Guan Y. (2019) An extremely heavy chlorine reservoir in the Moon: insights from the apatite in lunar meteorites. *Sci. Rep.* **9**, 5727.

Warren P. H. and Jerde E. A. (1987) Composition and origin of Nuevo Laredo trend eucrites. *Geochim. Cosmochim. Acta* **51**, 713–725.

Warren P. H., Kallemeyn G. W., Huber H., Ulff-Møller F. and Choe W. (2009) Siderophile and other geochemical constraints on mixing relationships among HED-meteoritic breccias. *Geochim. Cosmochim. Acta* **73**, 5918–5943.

Williams J. T., Shearer C. K., Sharp Z. D., Burger P. V., McCubbin F. M., Santos A. R., Agee C. B. and McKeegan K. D. (2016) The chlorine isotopic composition of Martian meteorites 1: Chlorine isotope composition of Martian mantle and crustal reservoirs and their interactions. *Meteorit. Planet. Sci.* **51**, 2092–2110.

Wilson R. M., Elliott J. C. and Dowker S. E. P. (1999) Rietveld refinement of the crystallographic structure of human dental enamel apatites. *Am. Mineral.* **84**, 1406–1414.

Yamaguchi A., Takeda H., Bogard D. D. and Garrison D. (1994) Textural variations and impact history of the Millbillillie eucrite. *Meteoritics* **29**, 237–245.

Yamaguchi A., Taylor G. J. and Keil K. (1996) Global crustal metamorphism of the eucrite parent body. *Icarus* **124**, 97–112.

Yamaguchi A., Barrat J. A., Greenwood R. C., Shirai N., Okamoto C., Setoyanagi T., Ebihara M., Franchi I. A. and Bohn M. (2009) Crustal partial melting on Vesta: evidence from highly metamorphosed eucrites. *Geochim. Cosmochim. Acta* **73**, 7162–7182.

Yamaguchi A., Mikouchi T., Ito M., Shirai N., Barrat J. A., Messenger S. and Ebihara M. (2013) Experimental evidence of fast transport of trace elements in planetary basaltic crusts by high temperature metamorphism. *Earth Planet. Sci. Lett.* **368**, 101–109.

Zhou Q., Yin Q.-Z., Young E. D., Li X.-H., Wu F.-Y., Li Q.-L., Liu Y. and Tang G.-Q. (2013) SIMS Pb–Pb and U-Pb age determination of eucrite zircons at <5μm scale and the first 50Ma of the thermal history of Vesta. *Geochim. Cosmochim. Acta* **110**, 152–175.

Associate editor: James M.D. Day